JMB

Nicotinic Acetylcholine Receptor at 4.6 Å Resolution: Transverse Tunnels in the Channel Wall

A. Miyazawa[1,2], Y. Fujiyoshi[3], M. Stowell[1] and N. Unwin[1]*

[1]*MRC Laboratory of Molecular Biology, Hills Road, Cambridge CB2 2QH, UK*

[2]*International Institute for Advanced Research, Matsushita Electric Industrial Co., Ltd. 3-4 Hikaridai, Seika, Kyoto 619-0237, Japan*

[3]*Department of Biophysics Faculty of Science, Kyoto University, Oiwake-cho Kitashirakawa, Sakyo-ku Kyoto 606-8502, Japan*

The nicotinic acetylcholine (ACh) receptor is the neurotransmitter-gated ion channel responsible for the rapid propagation of electrical signals between cells at the nerve/muscle synapse. We report here the 4.6 Å structure of this channel in the closed conformation, determined by electron microscopy of tubular crystals of *Torpedo* postsynaptic membranes embedded in amorphous ice. The analysis was conducted on images recorded at 4 K with a 300 kV field emission source, by combining data from four helical families of tubes ($-16,6$; $-18,6$; $-15,7$; $-17,5$), and applying three-dimensional corrections for lattice distortions. The study extends earlier work on the same specimen at 9 Å resolution.

Several features having functional implications now appear with better definition. The gate of the channel forms a narrow bridge, consisting of no more than one or two rings of side-chains, across the middle portion of the membrane-spanning pore. Tunnels, framed by twisted β-sheet strands, are resolved in the extracellular wall of the channel connecting the water-filled vestibule to the putative ACh-binding pockets. A set of narrow openings through which ions can flow are resolved between α-helical segments forming part of the cytoplasmic wall of the channel. It is suggested that the extracellular tunnels are access routes to the binding pockets for ACh, and that the cytoplasmic openings serve as filters to exclude anions and other impermeant species from the vicinity of the pore. Both transverse pathways are likely to be important in achieving a rapid postsynaptic response.

© 1999 Academic Press

Keywords: acetylcholine receptor; ion channel; tubular crystal; liquid helium; electron microscopy

*Corresponding author

Introduction

Nicotinic ACh receptors are ion channels found in high concentrations in the postsynaptic membranes of muscle cells, where they mediate the chemical transmission of electrical signals from invading motor neurons. ACh released at the synaptic junctions stimulates the channels to open, and the flow of cations through them rapidly depolarises the postsynaptic membrane of the muscle cell, initiating an electrical signal that causes the muscle to contract. Although the ACh receptor is by far the best characterised neurotransmitter-gated ion channel in terms of its biochemical, physiological and pharmacological properties (for recent reviews, see Lester, 1992; Karlin & Akabas, 1995; Changeux & Edelstein, 1998), the detailed structural mechanisms underlying the rapid depolarisation are not yet understood.

The ACh receptor is a large (∼290 kDa) glycoprotein complex. It is made from five membrane-spanning subunits: two (the αs) having identical amino acid sequences, and three others (β, γ and δ) having sequences homologous to the αs. The subunits have in common a large extracellular amino-terminal domain, four predicted transmembrane regions (M1-M4), and a substantial M3-M4 cytoplasmic loop. These are organised around a pseudo 5-fold axis that delineates a cation-selective pathway across the membrane when the channel is open, but a robust barrier to the ions when it is closed. Opening of the channel occurs upon binding of ACh to both α subunits at sites influenced most especially by the neighbouring γ and δ subunits. The site in α_γ (the α subunit next to the γ subunit) is distinguished biochemically from the site in α_δ (the α subunit next to the δ subunit) by its higher affinity for the competitive antagonist, *d*-

---

tubocurarine (Neubig & Cohen, 1979). α_γ and α_δ are separated by one subunit. Electron crystallographic studies, using subunit-specific labels, determined the intervening subunit to be β (Kubalek et al., 1987); other lines of evidence favour γ as the subunit in this location (Karlin, 1993).

Postsynaptic membranes isolated from the (muscle-derived) electric organ of the *Torpedo* ray are readily converted into tubular vesicles containing receptors arranged regularly on their surfaces, almost as they are *in vivo* (Heuser & Salpeter, 1979). These tubular crystals, or "tubes", have overall helical symmetry, making them an ideal kind of specimen for three-dimensional structure determination by electron microscopy. An initial electron microscopic study of tubes frozen to retain their helical symmetry (Toyoshima & Unwin, 1988) showed that the ring of five receptor subunits creates a narrow pore across the membrane, flanked on either side by ~20 Å wide vestibules. The vestibule on the extracellular side (outside of the tube) is ~65 Å long. The vestibule on the cytoplasmic side is shorter and has additional density underlying it. This density was not visible in tubes imaged in high pH solution and hence was attributed to the clustering protein, rapsyn, which is normally present in approximately 1:1 stoichiometry with the receptor in *Torpedo* postsynaptic membranes (Sealock, 1982; LaRochelle & Froehner, 1986), but is released by alkaline pH (Neubig et al., 1979).

A more recent study of the tubes revealed elements of secondary structure in the transmembrane portion of the receptor and also in a region ~30 Å away from the membrane, where the two α subunits contain cavities: the putative ACh-binding pockets (Unwin, 1993). The structures shaping the two cavities are similar but not identical, indicating that the α subunits have different conformations before ACh binds (Unwin, 1996). Additionally, a time-resolved analysis of the tubes showed that the receptor undergoes a concerted conformational change, involving disturbances around both cavities, after brief reaction with ACh to induce the open-channel form (Unwin, 1995). The gate near the middle of the membrane opens up as a result of this transition, and the pore becomes narrowest close to the cytoplasmic membrane surface.

The resolution in these recent structural investigations (~9 Å) was limited by the modest performance of the electron microscopes used and by distortions that caused the receptors to be displaced significantly from their correct lattice positions over distances beyond about 800 Å. Here, we have been able to record images of exceptional quality by using a 300 kV field emission electron microscope incorporating a top-entry liquid-helium-cooled stage (Fujiyoshi et al., 1991). We have also applied a computational method to correct in three dimensions for the lattice distortions (Beroukhim & Unwin, 1997), and analysed images from four helical families of tubes. The technical

improvements, and the collection of more extensive data, have allowed the structure determination to be extended to 4.6 Å resolution.

Here, we compare the receptor structures determined from the four helical families of tubes and show that these structures are equivalent. The four three-dimensional density maps could therefore be combined to obtain an average structure, contributed by more than 500,000 molecules. The average structure reveals, with better definition, the gate of the channel and features affecting ACh binding and ion transport. We now find that there are tunnels in the extracellular wall of the channel connecting the vestibule to the putative ACh-binding pockets. Structural parallels with the "gorge" in acetylcholinesterase suggest that these tunnels are access routes for ACh to the binding pockets. Narrow openings are also resolved in the cytoplasmic wall of the receptor, which may serve as filters to exclude anions and other impermeant species from the vicinity of the pore. Direct flow of ions into or from the interior of the cell appears to be obstructed not only by rapsyn, as originally thought, but also by a part of the receptor itself.

Results

Subdivision into helical families

ACh receptor tubes form from ribbons of receptor dimers (Brisson & Unwin, 1984). The ribbons associate side-by-side to make a surface lattice which in two dimensions would have the plane group symmetry, *p*2. The unit cell vectors of this lattice and the principal 1,0 and 0,1 lines are shown in Figure 1(a). To represent a tube, the same sets of lines may be considered as helical traces over the surface of a cylinder. They thus give rise to a range of helical families depending on the number of lines required to make up the cylinder's circumference. The helical family encountered most frequently was that having sixteen 1,0 lines (forming left-handed helices) and six 0,1 lines (forming right-handed helices) around the circumference. This family is denoted: $(-16,6)$. Other families also encountered in most preparations, and analysed in the present study, include $(-18,6)$, $(-15,7)$ and $(-17,5)$.

As indicated in Figure 1(b), ribbons of the $(-15,7)$ family have the longest helical pitch, whereas those of the $(-17,5)$ family have the shortest; ribbons of the $(-16,6)$ and $(-18,6)$ families have a similar pitch, but the $(-18,6)$ tube has a larger radius than the $(-16,6)$ tube because it has two extra 1,0 lines around the circumference. The variation in radius between the families is quite small: 380 Å, 385 Å, 394 Å and 416 Å for the $(-17,5)$, $(-16,6)$, $(-15,7)$ and $(-18,6)$ families, respectively.

The tubes have symmetry elements in addition to their basic helical construction. They all contain radial 2-fold axes, originating from the *p*2 surface lattice, and consequently appear centrosymmetric
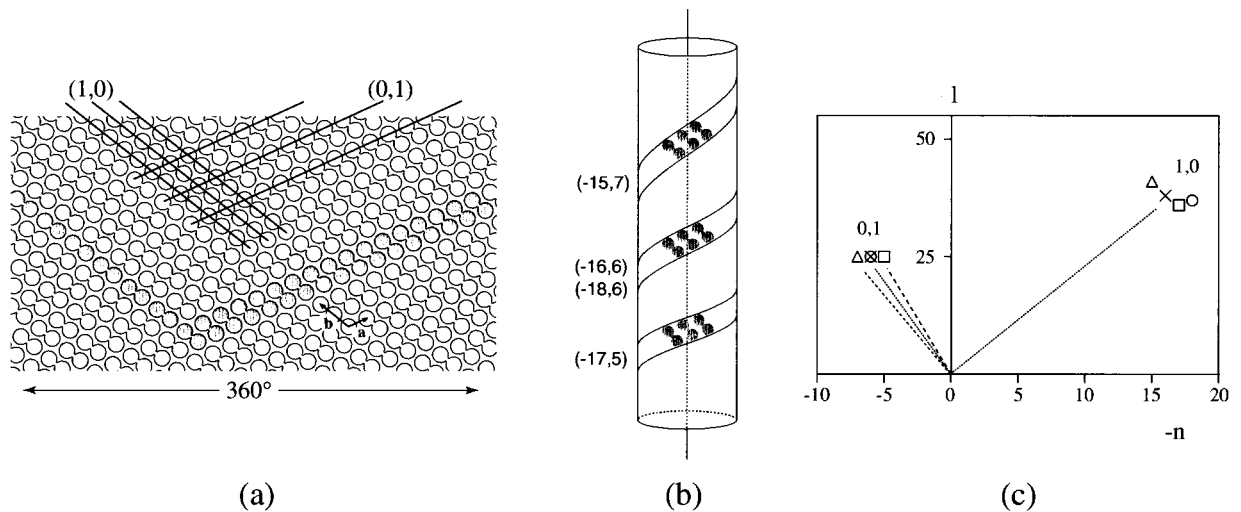
Figure 1. Subdivision of tubes into helical families. (a) Diagram of the surface lattice, made by opening up the cylindrical tube and viewing it from the outside. This lattice is built from ribbons of receptor dimers (linked circles), which run obliquely to the axis of the cylinder (vertical). The unit cell vectors and the principal 1,0 and 0,1 lines are indicated. The indices that characterise individual helical families are determined by the numbers of the two principal lines (helices) required to fill 360° of azimuth. In this example, there are sixteen 1,0 and six 0,1 lines; the family is therefore (−16,6). (b) The ribbons of receptor dimers form helices having slightly different pitches depending on the helical family and the precise dimensions of the unit cell. (c) Plot of layer-line number, l, against the helix start number, n, for the principal 1,0 and 0,1 lines of the four helical families (×, (−16,6); ○, (−18,6); △, (−15,7); □, (−17,5)). The close grouping of points indicates that the four surface lattices have similar dimensions and orientations with respect to the axis of the tube; the small variation in 0,1 positions reflects the small variation in helical pitch of the dimer ribbons.

in projection. In the case of the (−16,6) and (−18,6) families there are also 2-fold and 6-fold rotation axes, respectively, generated along the axis of the tube.

A general property of tubular crystals is that there is some variation in the helical pitch (or orientation of the surface lattice), even within a given helical family. This gives rise to variations in the relative positions of layer-lines in their diffraction patterns (i.e. to variations in tube type) and to a multitude of helical selection rules. To compare and combine Fourier terms from within a family it is usually necessary to reassign layer-lines to match those corresponding to a standard helical selection rule defining a typical set of positions in the diffraction pattern (see Methods). The standard selection rule used for the (−16,6) family was:

$$l = 113n' + 314m \quad (n = 2n')$$

where l is the layer-line number, m is an integer, n is the start number (i.e. number around the circumference) of the contributing helix, and $n = 2n'$ indicates that the start numbers occur in multiples of 2. This rule gives numbers of 38 and 25, respectively, for the principal (1,0; −16) and (0,1; 6) layer-lines ((h,k; n) notation; Toyoshima & Unwin, 1990). The standard selection rules for the other three families were:

$$l = 25n' + 112m \quad (n = 6n') \quad (-18, 6)$$
$$l = -91n + 662m \qquad\qquad (-15, 7)$$
$$l = 247n + 605m \qquad\qquad (-17, 5)$$

giving numbers for the principal layer-lines of 37 and 25 for (−18,6), 41 and 25 for (−15,7), and 36 and 25 for (−17,5). The clustering of points when the corresponding pairs of (n,l) indices are represented in an (n,l) plot (Figure 1(c); Klug et al., 1958) emphasises the close relation between the families (not made obvious by the selection rules).

Images and diffraction patterns

Images of tubes taken at 4 K with the field emission microscope (Figure 2(a)) look similar to conventional images. Striations visible across these tubes arise mainly from the extracellular ends of the receptors, which protrude radially outwards from the membrane surface. The striations may be specially prominent at the tube edges, depending on the helical family. The membrane itself and the cytoplasmic portion of the receptors are less visible, being obscured by the matter at higher radius.

Diffraction patterns from the images consist of closely spaced lines of continuous intensity (layer-lines) running perpendicular to the tube axis. The layer-lines fade out at a resolution of only ∼25 Å (Figure 3), as found with conventional images (e.g. see Toyoshima & Unwin, 1990), giving little direct evidence of improvement brought about by the lower recording temperature and more coherent electron beam. However, the tubes contain long-range distortions (bending, scale changes, variable tilt and
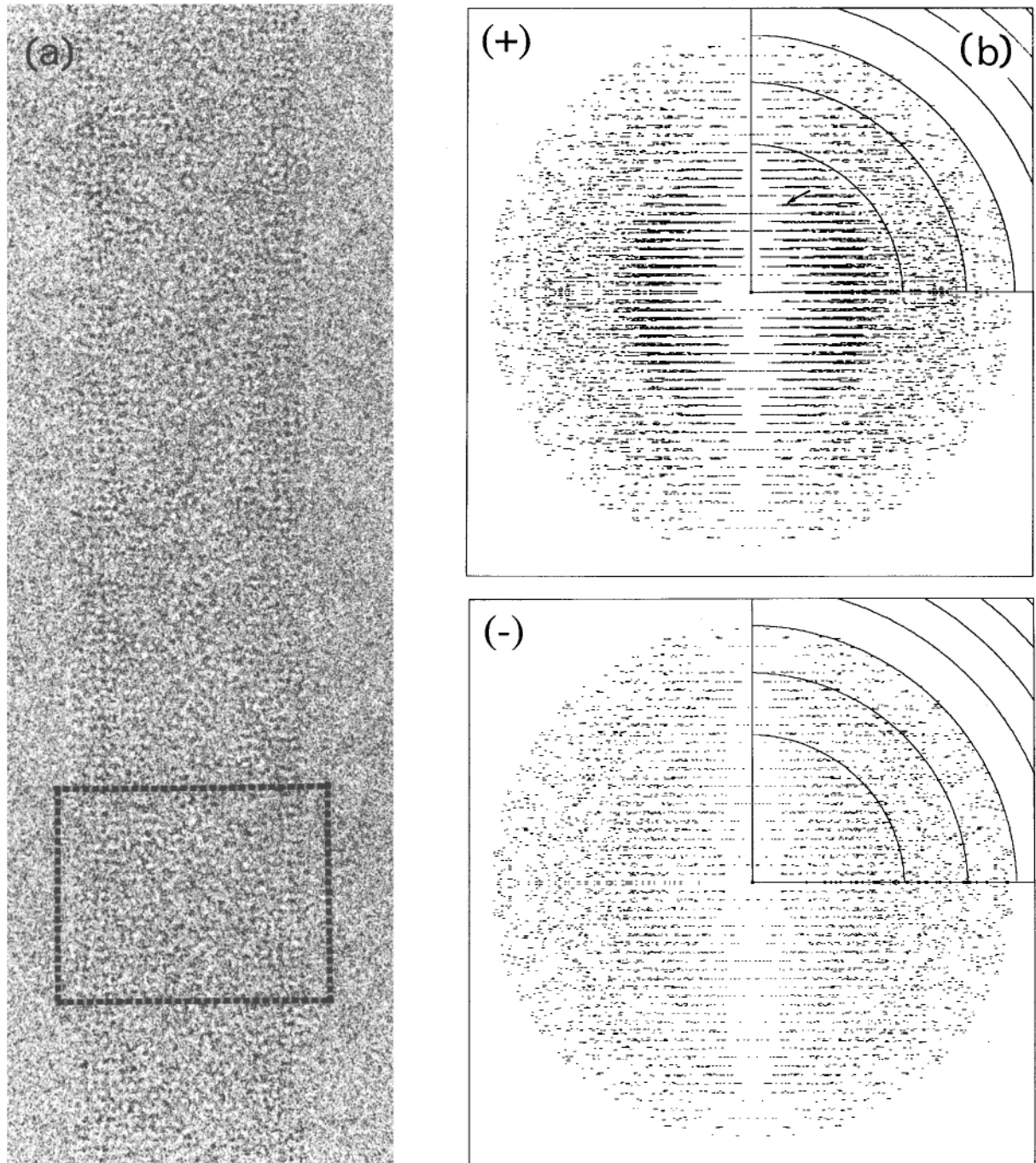
Figure 2. Image (a) and layer-line plots (b) obtained from a tube of the (−18,6) helical family (620497; Table 1). The tube is in amorphous ice over a hole in the carbon support film; the rectangle drawn over the tube, and extending over a length corresponding to 700 Å, indicates the typical size of a segment used in correcting distortions. The layer-line plots, from the distortion-corrected tube, highlight those Fourier terms having the same phase ((+); upper) and opposite phase ((−); lower) compared with those of the reference structure. Concentric rings drawn over quadrants in the two plots indicate the positions of the zeros of the CTF (mean underfocus, 14,980 Å). The CTF was refined by maximising the number of terms in the (+) plot while minimising the number in the (−) plot. The data shown are from the near side only of the tube, and in both plots the unique Fourier terms were included together with their mirror images across the meridian, giving the appearance of the Fourier transform of both sides of the tube. The arrow points to the (0,5; 30) layer-line (see Figure 3) ; these plots extend only to a resolution of $1/10$ Å^{-1}.

twist), which incur large displacements of molecules away from their exact lattice positions over long distances, and blur the diffraction at higher resolution, making it impossible to reveal this information directly.

Importantly, the background in the diffraction patterns shows strong modulations due to the contrast transfer function (CTF), which extend beyond the layer-lines and hence enable good estimates of the CTF to be made. The CTF is refined accurately
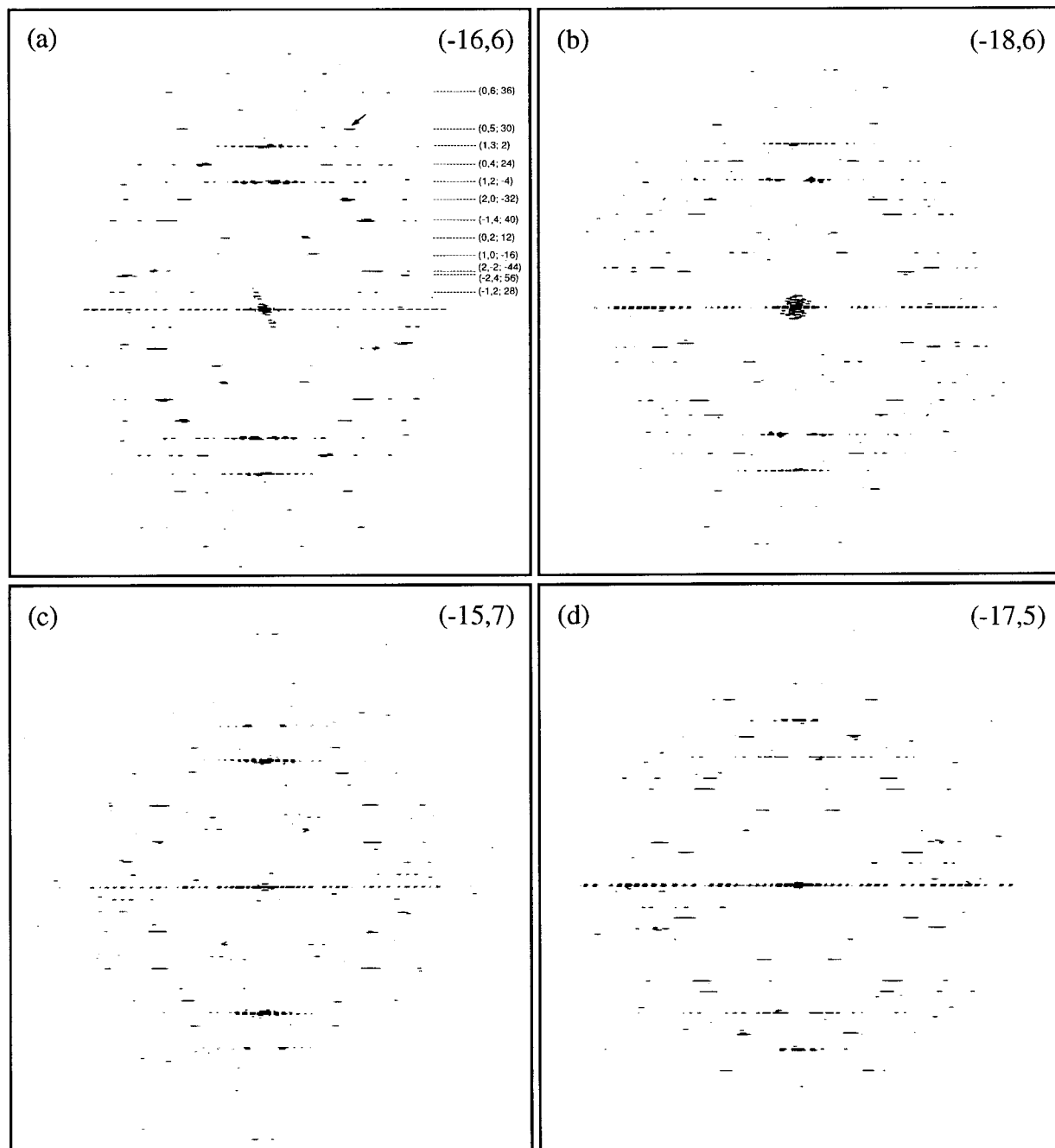
Figure 3. Comparison of computed diffraction patterns from the four families: (a) ($-16,6$); (b) ($-18,6$); (c) ($-15,7$); (d) ($-17,5$). Some of the major layer-lines in (a) are identified by their (h,k; n) indices; equivalent layer-lines in the other diffraction patterns have the same h,k indices, but may have different values for the Bessel order, n (for example, the ($1,2$; -4) layer-line in (a) is equivalent to the ($1,2$; -6), ($1,2$; -1), and ($1,2$; -7) layer-lines in (b), (c) and (d), respectively). The resolution of the ($0,5$; 30) peak in (a) (arrow) is $1/35$ Å^{-1}.

from the phases after distortion correction (see Methods), when many more layer-lines have become apparent. Figure 2(b) gives an example of the layer-line plots obtained by comparing the image phases with those of the reference dataset during the refinement.

Each family of tubes gives rise to a distinct diffraction pattern (Figure 3), determined by the numbers of principal 1,0 and 0,1 helical lines around the tube circumference and by the orientation of

the surface lattice. Within a family, the layer-line positions also vary slightly, leading to a range of tube types, each characterised by a particular helical selection rule (Figure 4). Because the molecular structure associated with each family is built up from a distinct set of helical density waves, data from separate families are combined most simply by averaging in real space, rather than in reciprocal space, as is done when data from the same family are combined.
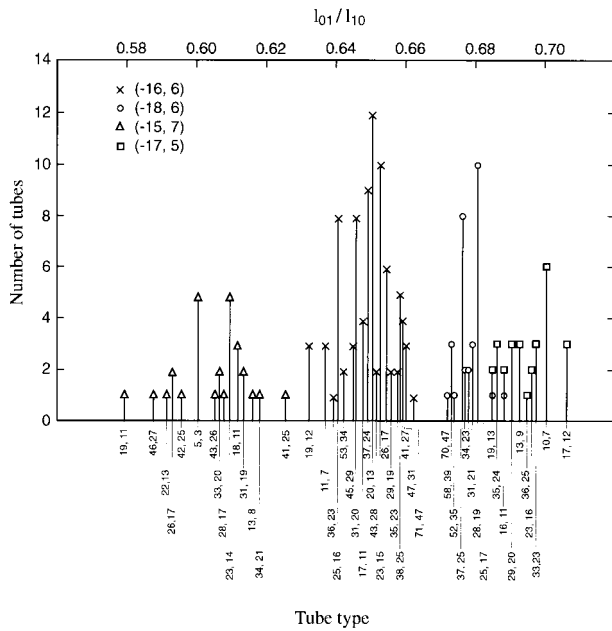
Figure 4. Histograms of the tube types present in the four helical families. The tube types are identified by the numbers of the principal 1,0 and 0,1 layer-lines, and plotted as ratios: $l_{0,1}/l_{1,0}$. Each type is characterised by a particular helical selection rule and gives rise to a particular pattern of overlapping Bessel terms.

Division into segments

The method we use here to measure and correct the distortions, and hence extract the higher resolution information, divides repeat lengths along the tubes into successive short segments and aligns each segment independently to a reference structure. By analysing shortened stretches, the displacements of molecules away from their correct lattice positions are reduced and so have a less significant effect. At the same time, the stretches need to be long enough for the whole repeat to be reconstructed accurately after the individual alignments have been worked out.

A preliminary investigation of the properties of distortions present in the tubes (Beroukhim & Unwin, 1997) suggested that the segment length should be roughly equal to the tube diameter for optimal extraction of the higher-resolution information. With segments much longer than this, the variations along the tube become smeared out (poor local fitting); with even shorter segments, the gain resulting from improved fitting to the reference structure begins to be outweighed by increased alignment errors. All tubes examined in the current study were divided into segments of lengths: 630-990 Å, the actual value chosen for a particular tube being influenced to some degree by the focus level (which affects the signal-to-noise ratio) and the axial repeat distance (which is divided into an integral number of segments). Table 1 lists the segment lengths used, together

Table 1. Details of the (−18,6) images

Film no.	Defocus (Å)	Tube length (Å)	Repeat length (Å)	Segment length (Å)	No. of receptors
611662	18,792	7947	2498	833	2924
611775	18,228	8987	3655	731	3307
611827	18,335	6559	3669	734	2414
611835	19,267	6085	3355	671	2239
620304	14,678	8436	3367	674	3104
620325	14,956	6565	2519	840	2416
620471	14,473	6783	1897	632	2496
620491	14,808	10,069	2529	843	3705
620497	14,980	7432	2493	831	2735
650523	13,546	3439	2787	929	1266
630037	14,242	9153	2556	852	3368
640171	12,715	10,173	3673	735	3744
650307	12,681	7826	1605	642	2880
670733	11,677	9218	2782	695	3392
670810	11,553	6560	3053	763	2414
670837	10,074	7158	5031	839	2634
670856	11,939	7134	3624	725	2625
670872	11,614	5409	2744	915	1991
670296	9643	3912	3004	751	1440
720355	10,630	5795	3635	727	2133
770186	14,515	5931	5801	967	2183
770192	15,741	6356	5706	713	2339
770197	15,512	6460	2482	827	2377
790148	12,279	8562	5637	705	3151
790213	11,452	5968	2457	819	2196
790263	13,054	14,809	6917	692	5450
790335	14,651	7959	3672	734	2929
860151	14,560	8379	2573	843	3083
860158	13,901	6256	3656	731	2302
860174	13,607	14,831	3727	745	5458
860195	14,954	7063	2514	838	2599
860340	11,835	10,718	2528	843	3944

with the defocus levels and axial repeat lengths, in the case of one of the helical families, (−18,6). Similar parameters were obtained with tubes in the other families.

Averaging tubes of the same family

The distortion-corrected images of tubes in the same helical family were averaged in reciprocal space (see Methods). Examination of the Fourier terms along the layer-lines, which are ideally those of a centrosymmetric object, allowed simple, continuous assessment of the data. It was observed, for example, that the signal-to-noise ratio (measured by PQ number; see Methods) improved approximately in proportion to the square-root of the number of images (Figure 5). Thus with a single image, there was too much noise for few, if any, of the layer-lines to be distinguished convincingly beyond a resolution of about 20 Å. However, after a large number of images had been averaged, the phases of the major peaks along most layer-lines became close to the ideal values of $0°$ or $180°$, indicating that a good signal-to-noise ratio had been achieved. Figure 6 shows examples of typical final amplitude and phase variations, obtained along layer-lines of the (−16,6) family. The layer-line in Figure 6(a) is at low axial resolution, but contains high Bessel order terms ($n = 206$); the layer-line in Figure 6(b) is intermediate in terms of resolution and Bessel order; the layer-line in Figure 6(c) is at high axial resolution (6.8 Å). The predominantly centrosymmetric character of the phases along these layer-lines demonstrates that the good signal-to-noise level extends in all directions to the limit of the Fourier transform.

After the tubes in each family had been averaged, three-dimensional maps were calculated so that the four independent structures could be aligned and averaged in real space to generate a structure of the receptor derived from all the images (see below). An alternative method for accomplishing the averaging, by combining the Bessel terms (g_{nl}) describing each structure (DeRosier et al., 1999), was not appropriate at the resolution of this analysis because the four surface lattices had significantly different unit cells.

Alignment of families

To align the four receptor structures, a single receptor was masked out from the (−16,6) map and used as a reference for pairwise comparison with receptors masked out from the other three maps. Each masked-out receptor was calculated in successive 1 Å spaced (x,y) sections, tangential to the axis of the tube, after first being centred on a radial line normal to the plane of the sections. Initial results from the pairwise comparisons showed that there were no significant systematic variations in the (x,y) translations needed to
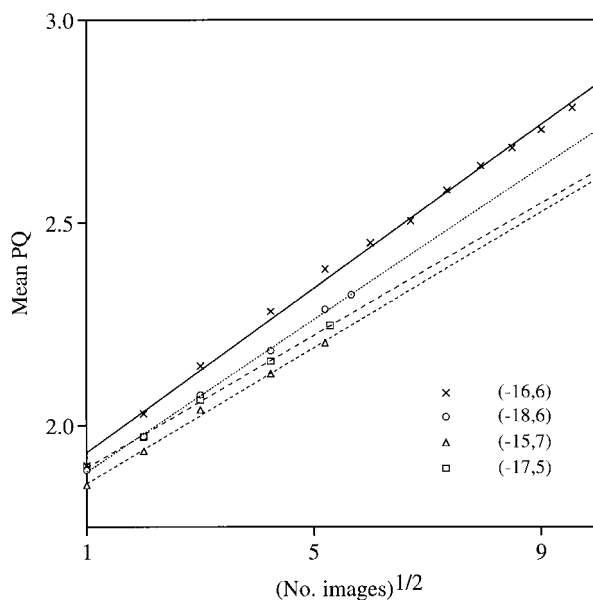

Figure 5. Mean PQ numbers (i.e. signal-to-noise ratios; see Methods) increase approximately linearly with the square root of the number of tube images averaged. Straight lines drawn through data points (least-squares fit), suggest that the families differ slightly in their signal-to-noise characteristics, and that the (−16,6) family provides the most well-ordered tubes.

achieve optimum correlation of sections at different levels in the structure. This was true for each family, examined in turn. Hence, the receptors were not tilted differently relative to the membrane plane, making it necessary to determine for each receptor pair only the rotational and translational alignments about and along a common central axis normal to the axis of the tube. Figure 7(a) and (b) plots the mean correlation coefficients measured from the sections in the refinement of the three families to the (−16,6) structure. The rotations and axial translations needed to achieve best alignments, obtained from the peaks in these curves, were: −1.6° and +31 Å; +3.1° and +9 Å; −2.4° and −4 Å for the (−18,6), (−15,7) and (−17,5) families respectively.

The maximum values for the correlation coefficients in Figure 7 (0.60, 0.52 and 0.54 for the (−18,6), (−15,7) and (−17,5) families) vary qualitatively in the way one would expect, considering the differences in numbers of receptors contributing to the individual maps (Table 2).

Correlation and statistics

Fourier shell correlation and phase residual measurement of the agreement between the masked-out, aligned receptors was used to measure the reliability and resolution of the structures determined for the four families. First, each of the four structures was evaluated by dividing the datasets into independent halves, and comparing the maps calculated from these
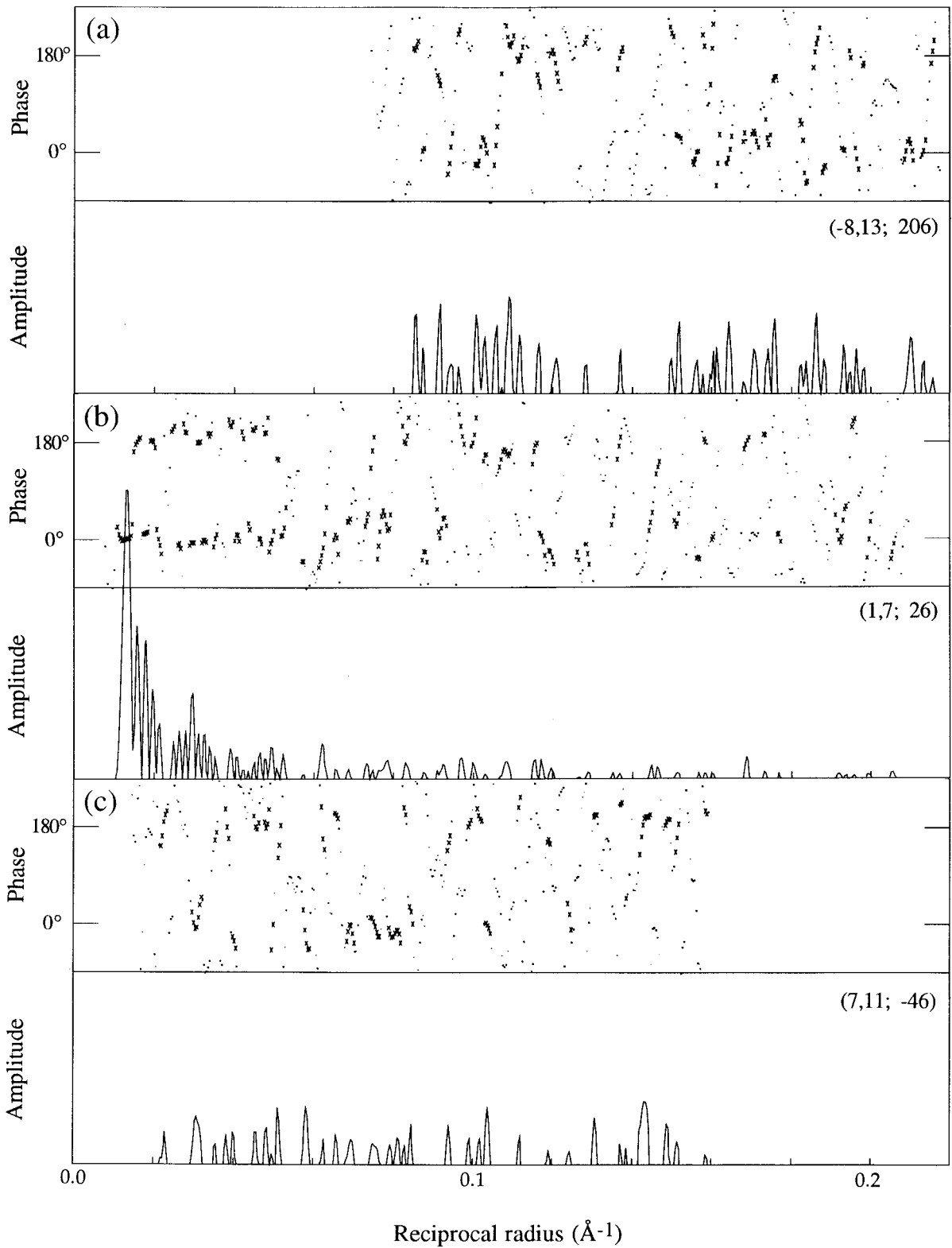
Figure 6. Phase (upper panels) and amplitude (lower panels) variations along three layer-lines from the (−16,6) family of tube. Indices (*h,k*; *n*) are shown; the axial resolutions of the layer-lines are: (a) 174 Å, (b) 17.2 Å and (c) 6.8 Å. Fourier terms above background (*PQ* > 1) and below background are identified by crosses and dots, respectively. Note that the phases of most terms are close to the ideal values of 0° or 180° where the amplitudes are strong, even with layer-lines having high Bessel orders and high axial resolution. The amplitudes in (a) and (c) are scaled five times relative to those in (b).
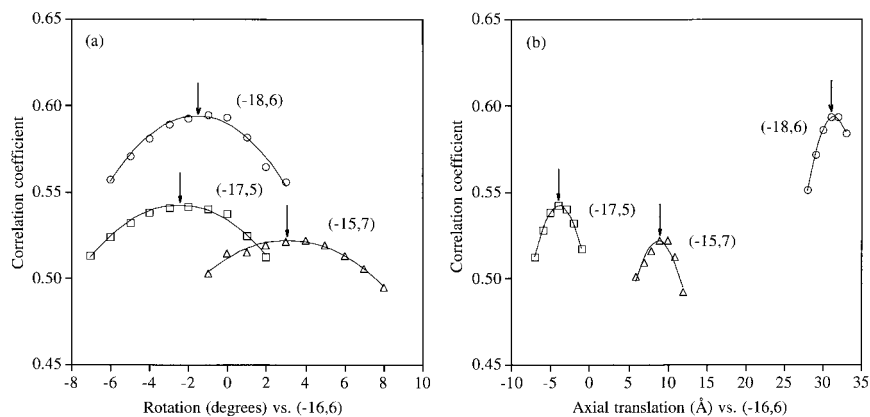
Figure 7. Determination of (a) the rotational alignment and (b) the axial alignment (normal to the tube axis) of masked-out receptors in each family by pairwise correlation of three-dimensional maps against the map calculated for the (−16,6) family. The correlations were calculated in successive 1 Å spaced (x,y) sections tangential to the axis of the tube (i.e. along the axes of the receptors), using a small positive cut-off density, after first optimising the (x,y) translational alignments between the pairs. The results shown refer to the mean correlation coefficients measured from all sections. Although the degree of correlation achieved reflects to some extent the density cut-off values used in the calculations, the peak positions and relative values remain largely unaffected. The arrows at the peaks of the curves identify the points of optimal alignment.

half-sets (Figure 8(a)). Each structure yielded a similar profile of correlation coefficient against resolution, with values improving approximately in proportion to the number of images included in the average. Next, the structures were evaluated by comparing the fully averaged (−16,6) map with the remaining three (Figure 8(b)). Again, each comparison yielded a similar set of curves, with improvements related to the number of images included in the average. Thus when all the images were averaged in independent groups and compared in these alternative ways (uppermost curves in Figure 8(a) and (b)), further significant improvements were obtained. For the final comparisons, the correlation coefficients fell to 0.3 (phase residual, 60°) at a resolution of 4.6 Å, the limit assumed for the present analysis.

Table 2 summarises details of the four 4.6 Å resolution datasets, obtained from a total of 178 images (534,426 receptors). Each dataset has been derived from more than 80,000 receptors, in tube segments of 700-800 Å mean length, and contains a full set of layer-lines (~1040) with >70,000 independent Fourier terms. The maximum Bessel order of these terms is 570. Most of the images have come from the (−16,6) family, the one most frequently encountered. The higher quality of the data from this family is due mainly to the greater

number of segments incorporated into the average. However, the signal-to-noise properties of the four families are not exactly equivalent when numbers of images (segments) are taken into account (Figure 5), and it appears that tubes of the (-16,6) family are inherently slightly better than the others.

Radial density distributions

Figure 9(a) shows the mean radial density distributions (g_{00}) calculated by Fourier-Bessel inversion of the terms from the averaged, CTF-corrected equatorial layer-lines of each family. The curves exhibit five maxima (I-V) of approximately equal relative strengths, and become in register (Figure 9(b)) after they have been shifted according to the alignments indicated Figure 7(b). Maxima I and II were not separately resolved in the earlier studies, and were together attributed to the receptor-clustering protein, rapsyn (Toyoshima & Unwin, 1998). The present study suggests, however, that only component I is likely to be rapsyn, whereas component II is a part of the receptor itself (see below). The remaining maxima (III, IV and V) can be identified with the phospholipid headgroup regions of the lipid bilayer and density composing the extracellular domain (Toyoshima & Unwin, 1998, 1990).

Table 2. Comparison of families

Family	No. of images	No. of receptors	Mean segment length (Å)	Layer-lines	Independent Fourier terms	Phase residual[a] (degrees)
(−16,6)	91	277,904	741	1038	76,976	9.9
(−18,6)	32	91,239	774	1052	73,816	14.1
(−15,7)	27	83,228	769	1042	71,969	15.3
(−17,5)	28	82,055	753	1054	74,846	14.7

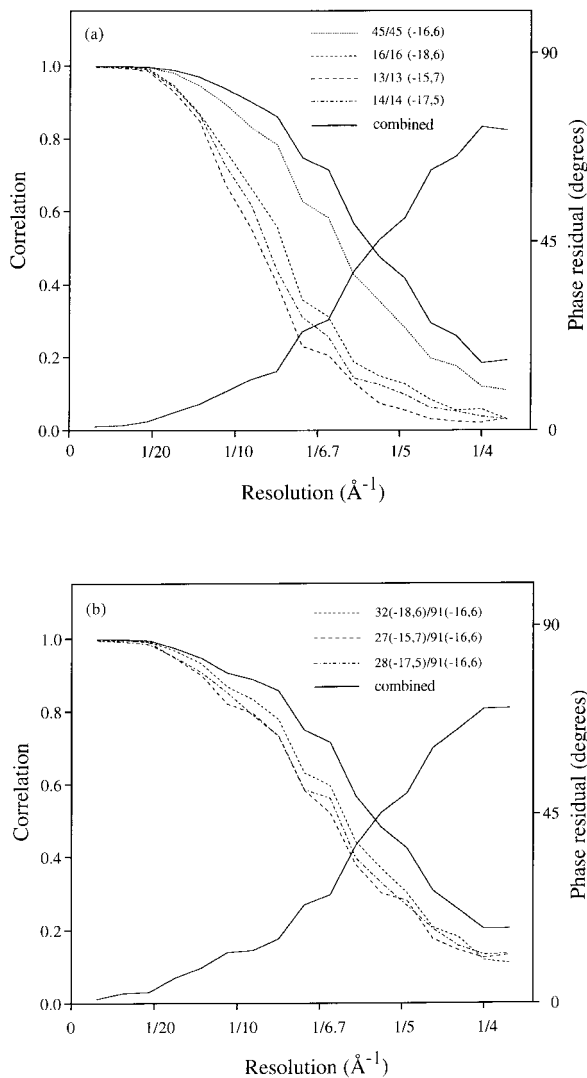[a] Amplitude-weighted phase deviation from the nearest of 0° or 180°.

Figure 8. Fourier shell correlations showing pairwise comparisons between the receptor structures calculated for the different families. (a) An evaluation of individual families obtained by comparing maps derived from independent half-sets of data. (b) A comparison of the fully averaged (−16,6) structure with the averaged structures determined from the other three families. The uppermost curves in (a) and (b), yielding the best correlation values, were obtained by comparing the four families averaged together in independent half-sets, and by comparing the fully averaged (−16,6) structure with the average of the remaining three; also shown are the Fourier shell phase residuals for these two cases. The numbers of images included in each comparison are indicated in the panels.

Comparison of three-dimensional maps

Figure 10(a)-(d) shows cross-sections of the tubes calculated from the four family datasets, with the g_{00} terms in Figure 9 included. The examples each show two concentric rings of roughly equal density (30 Å apart), which arise from the headgroups of the lipid bilayer. Otherwise each section has a distinct appearance, brought about by the different

helical parameters. Individual receptors in these sections are intersected at locations determined by the precise orientation of the surface lattice and by the symmetry elements present, and therefore do not all appear the same. In some cases, the cation-conducting pathway is presented in profile (arrow in (a)); in others, the subdivision of the cytoplasmic densities into two components (I and II in Figure 9) is clearly visible (pair of arrows in (b)).

Structure of the receptor

A structure of the receptor having optimal signal-to-noise ratio was obtained by calculating an average of the four independently determined maps. This structure, in terms of overall appearance and the identified secondary structural elements, resembles the one described previously (Unwin, 1993). However, the cation-conducting pathway and certain other details are now better defined. Particularly striking at 4.6 Å resolution are narrow openings in the wall of the receptor close to the cytoplasmic membrane surface, making transverse passages for the ions, and tunnels connecting the water-filled vestibule to cavities in the extracellular portions of the two α subunits. As discussed below, the cavities appear to be the ACh-binding pockets and the tunnels the routes by which ACh gains access to them.

A description of the main new features begins with the cation-conducting pathway. This lies centrally along the axis of the receptor for most of its length. Figure 11 shows its shape in cross-section, viewed from 5-fold related directions intersecting the α_δ, β and α_γ subunits successively (as indicated by the icons). Common to all views are the ~20 Å wide vestibules on either side of the membrane, and a more constricted membrane-spanning pore. The pore is bridged from all angles by a narrow strip of density near the middle, but slightly towards the cytoplasmic side, of the membrane. Since there are no other comparable regions that would constitute a total barrier to the ions, the bridging density must correspond to the gate of the channel.

The cytoplasmic end of the receptor presents a further constriction to the passage of ions. They are prevented from flowing directly into (or from) the cell interior by the central mass at the base of the receptor, and must instead pass through narrow transverse openings now resolved in the channel wall (Figure 11(a), arrow). Figure 12(a) and (b) shows how the openings are made: they lie between rods, which project down from each subunit and come together beneath the receptor to form an inverted pentagonal cone. Each of the cone-shaping rods appears to contain an α-helix that is about 30 Å long. There are two major openings, lying on opposite faces of the two α subunits (Figure 12(b), arrows), and although none of them is more than about 8 Å across at its widest point, they are up to ~15 Å long. Together, therefore,
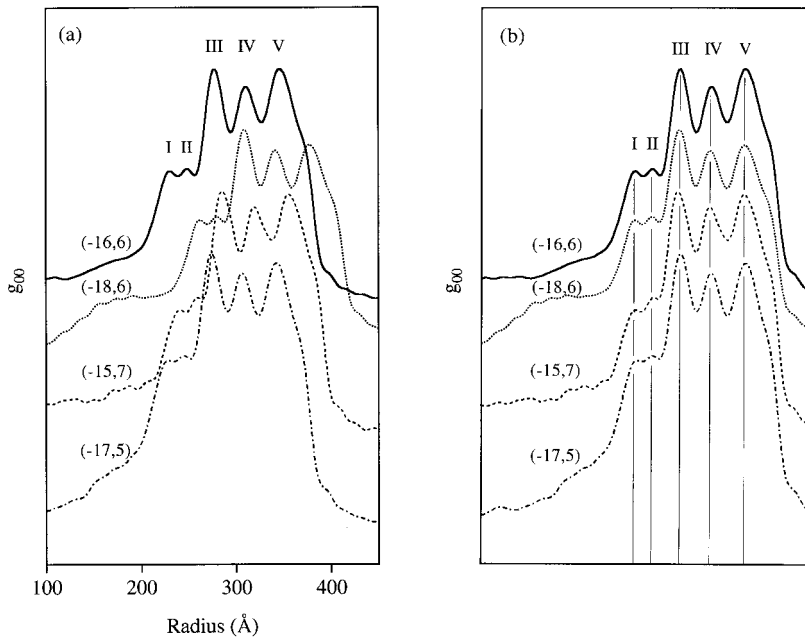
Figure 9. Variations in mean density (g_{00}) obtained by Fourier-Bessel inversion of the terms along the averaged, CTF-corrected equatorial layer-lines of each helical family. In (a) the variations are plotted as a function of radial distance from the tube axis; each curve shows five distinct maxima (labelled I-V). In (b) the individual curves have been shifted relative to one another by the amounts indicated in Figure 7(b) to account for the differences in tube diameters. The maxima, I-V, which are now in register, can be identified with different components of the subsynaptic membrane (see the text).

they create an extensive cross-sectional area through which the ions could pass.

The pentagonal features at the base of the receptor extend only to the level indicated by the horizontal line in Figure 11(b); that is ~40 Å from the cytoplasmic membrane surface (see also Figure 12(a)). Below this level there are no 5-fold related densities, but instead a strong indication of 2-fold symmetry (Figure 12(a), bottom). Hence, matter at the extreme end of the receptor
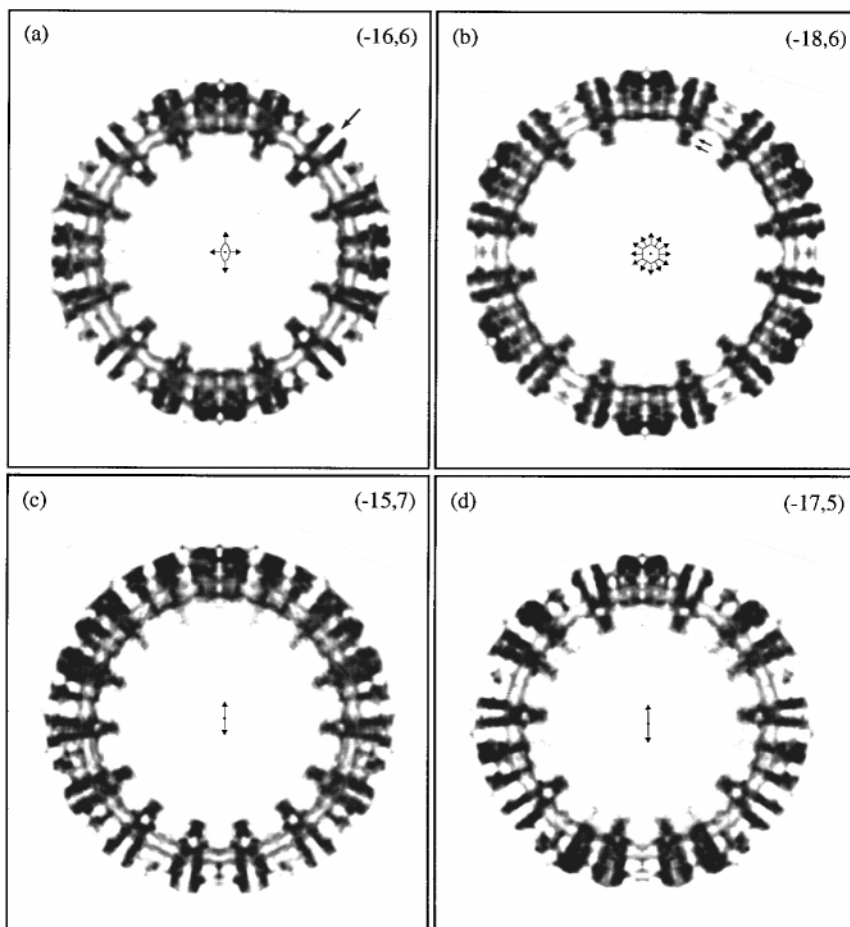

Figure 10. Cross-sections calculated through tubes of the: (a) (−16,6); (b) (−18,6); (c) (−15,7) and (d) (−17,5) helical families. Radial 2-fold axes in the plane of these sections give rise to mirror symmetry. The (−16,6) and (−18,6) families have additional 2-fold and 6-fold rotational axes running along the axis of the tube. Concentric rings of density, 30 Å apart, identify the phospholipid headgroup regions associated with the inner and outer leaflets of the lipid bilayer. The arrow in (a) points to a receptor cut approximately along its central axis, revealing the profile of the ion pathway; the pair of arrows in (b) indicate subdivision of densities at the cytoplasmic end of the receptor (corresponding to maxima I and II in Figure 9). Only Fourier terms to a resolution of 10 Å have been used for these displays. The sides of the frames correspond to 960 Å.
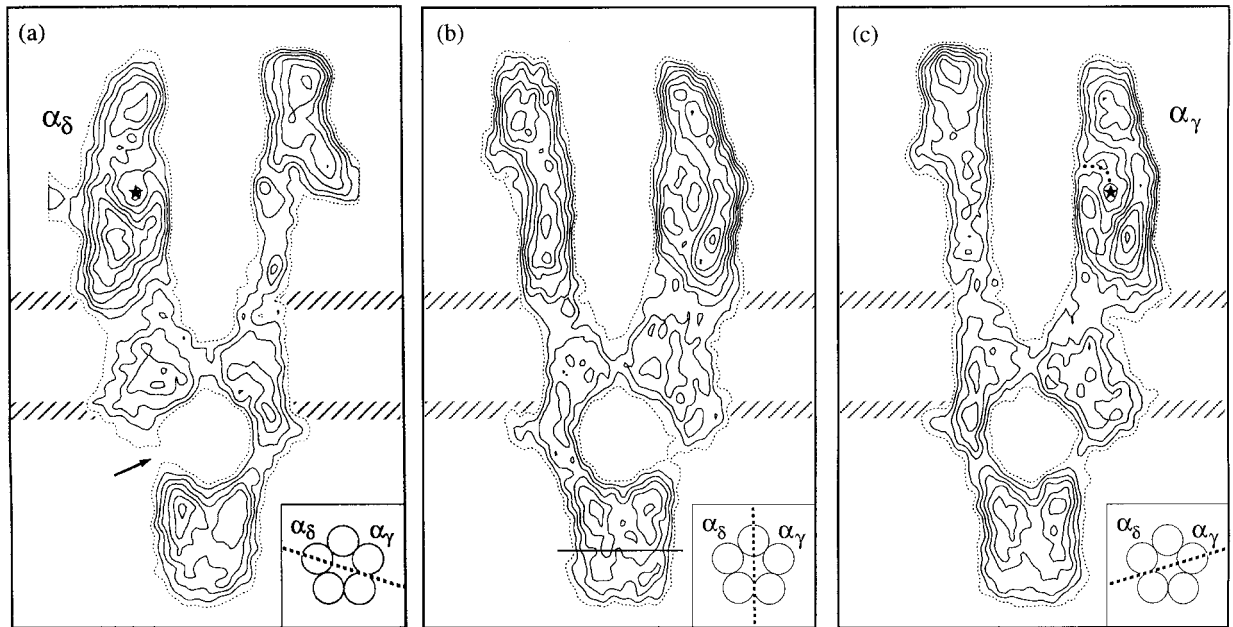
Figure 11. Cross-sections through the fully averaged structure running along the central axis of the receptor, and rotated about this axis to bring in successive 5-fold related views. (a), (b) and (c) intersect, respectively, the α_δ, β and α_γ subunits, as indicated by the icons (subunit assignments, see Kubalek *et al.*, 1987). Asterisks in (a) and (c) identify cavities in the extracellular portions of the α subunits where ACh is thought to bind; narrow tunnels (dotted line in (c)) connect these cavities to the vestibule of the channel (see also Figure 13). The arrow in (a) points to an opening in the channel wall on the cytoplasmic side of the membrane (see also Figure 12(a) and (b)). The horizontal line in (b) indicates the lower extent of 5-fold-related densities; matter below this level shows a strong indication of 2-fold symmetry and therefore appears to be non-receptor protein. The cytoplasmic openings are at the subunit interfaces, the locations of which are rotated slightly relative to their locations at the level ($\sim$30 Å above the membrane) of the icons. The positions of the phospholipid headgroups are indicated by the pairs of horizontal bands (30 Å centre-to-centre separation) in each of the panels.

(corresponding to component I in Figure 9) probably does not represent part of the receptor itself, but more likely originates from another protein (rapsyn), equivalent portions of which link together underneath.

The cavities observed in the extracellular portions of the two α subunits (asterisks in Figure 11(a) and (c)), are not apparent in the other subunits (e.g. see Figure 11(b)), and lie centrally within the α subunits at a location about 50 Å away from the channel gate. The dimensions and shapes of the cavities are similar but not identical (Figure 11(a) and (c); Figure 12(c)), and their upper regions connect to the water-filled vestibule by narrow, 10-15 Å long tunnels running through the channel wall (dotted line in Figure 11(c)).

Both tunnels opening into these internal cavities are shaped mainly by strands of β-sheet running roughly perpendicular to the membrane plane. Figure 13 is a cross-section normal to the channel axis at the top of the dotted line in Figure 11(c), showing the peaks of density ($\sim$4.7 Å apart) associated with the inter-chain spacing of the β-sheet and the tunnels (arrows) in α_γ and α_δ, which are continuous with the water-filled vestibular space. There are crescents of about seven such peaks and some additional tunnel-lining densities that are characteristic of both α subunits, distinguishing them unambiguously from the other

three subunits. Both tunnels therefore lie within the α subunits. The small differences in appearance of these tunnels, the surrounding densities and the cavities reflect the different conformations of the two α subunits in the closed-channel form of the receptor.

Figure 14 shows a 15 Å thick slab through the regular β-sheet densities framing the tunnel in the α_γ subunit. Seven strands are visualised, corresponding to the seven peaks labelled in Figure 13. The sheet displays the normal right-handed twist, with strands 2-4 running almost perpendicular to the membrane plane for most of their length and those on either side being more strongly tilted.

Discussion

The results presented above have led to a description of the high-resolution structure of the closed-channel form of the ACh receptor. Four helical families of tubular crystals were examined: the one most frequently encountered, ($-$16,6), and three others having the same surface lattice, but different helical parameters. We showed by pairwise correlation that three-dimensional maps of the receptor obtained from each family were essentially the same, when differences in numbers of images were taken into account, and therefore that the densities could be averaged directly to obtain a
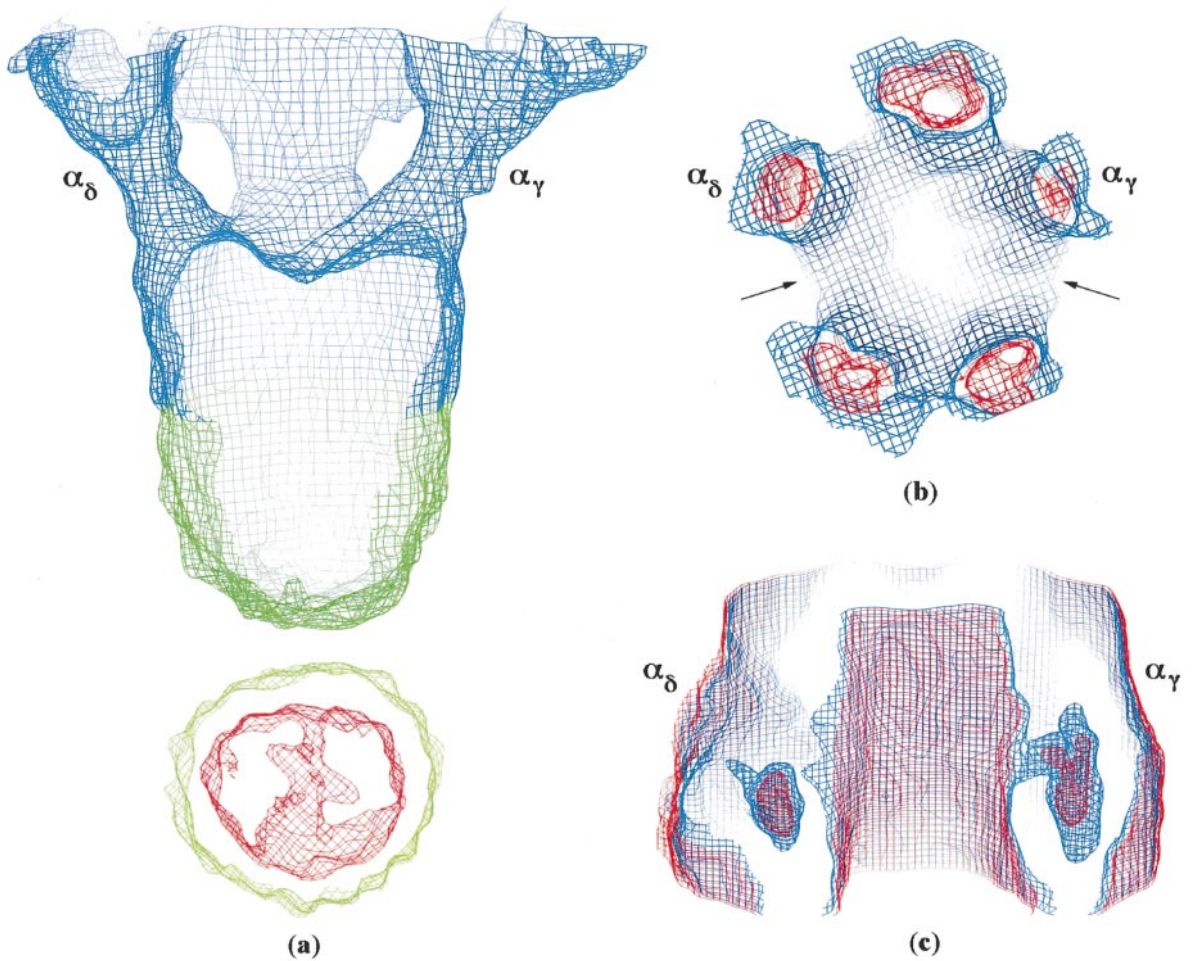
Figure 12. Three-dimensional views obtained from the fully averaged structure. (a) A cut through the cytoplasmic portion of the receptor to allow an unobstructed view of three of the rods that protrude from each of the subunits and come together on the receptor axis, forming an inverted pentagonal cone; underneath the rods are additional 2-fold-related densities (green), most likely originating from rapsyn (see the text). (b) A view from inside the cytoplasmic vestibule of the narrow openings made between these rods; arrows point to the two major openings (the left arrow points to the same opening as indicated by the arrow in Figure 11(a)). (c) A cut through the extracellular portion of the receptor showing the putative ACh-binding pockets in the two α subunits, which connect by tunnels to the central vestibule; the α_δ tunnel is more constricted than the one in α_γ, and is not revealed at the threshold chosen (see also Figure 11(a) and (c); Figure 13). The α_γ and α_δ subunits are labelled in each part of the Figure. The contours are at 2.0 and 2.3σ (the lowest contours being blue/green in (a) and (b), but red in (c)), and the net spacing corresponds to 1 Å.

resultant structure having optimal signal-to-noise ratio. Altogether, 178 images contributed to the structure determination, making it a much more extensive analysis than had been undertaken in earlier studies of the receptor.

The greater number of molecules incorporated into the average, combined with images of better quality and the use of a three-dimensional distortion correction procedure, produced a significant improvement in resolution compared with the earlier work. Consequently, it has become possible to discern the inter-chain periodicity of β-sheet in some regions of the structure (Figures 13 and 14), to observe functional components of the ion channel with better definition, and to obtain new insight into the architecture and physiological properties of the sub-synaptic membrane.

A proper chemical interpretation of the structure should become available as soon as it is feasible to trace reliably the polypeptide chains through the three-dimensional densities. At this stage, we have restricted our attention mainly to four regions of the receptor that have obvious functional significance and about which reasonable interpretations can now be made. These are the putative ACh-binding pockets in the two α subunits, and tunnels connecting them to the external medium; the gate within the membrane, creating a physical barrier to the flow of ions; the cytoplasmic wall, through which ions must pass when the channel opens; and the cytoplasmic end of the receptor, to which the clustering protein, rapsyn, appears to bind.
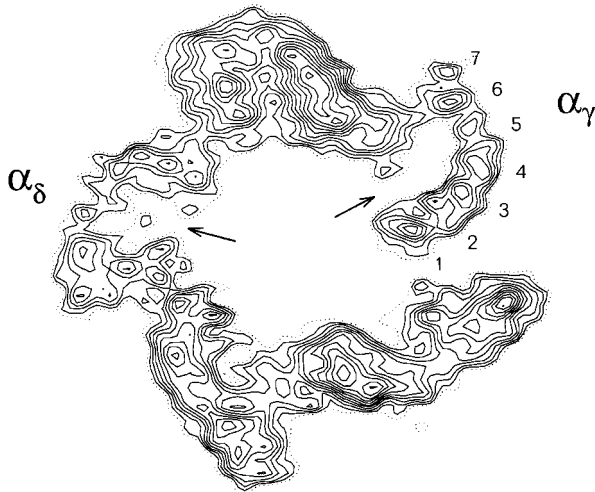
Figure 13. Section through the fully averaged structure parallel to the membrane plane, showing the tunnels (arrows) that connect the extracellular vestibule of the channel to cavities (the putative ACh-binding pockets) within the α_γ and α_δ subunits. The regular patterns of density lining both tunnels arise from strands of β-sheet (labelled 1-7 on α_γ) running approximately normal to the membrane plane. The level of the section is at the top of the dotted line tracing the tunnel in Figure 11(c). The appearance of the β-sheet in this section (and also in Figure 14) has been enhanced by including Fourier terms to 3.8 Å resolution in the calculations.
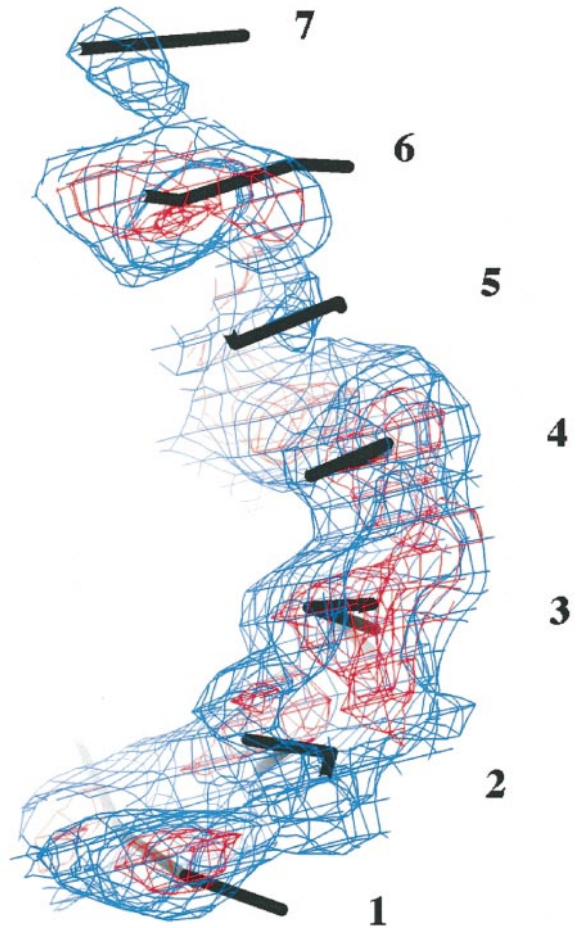
Tunnels to the ACh-binding pockets

The extracellular domains of both α subunits contain cavities that were proposed in an earlier study to be the ACh-binding pockets (Unwin, 1993). This assignment was based on two lines of evidence. First, the two ACh-binding α subunits were the only subunits found to contain these specialised internal features. Second, the cavities aligned, in projection, with the locations of the binding sites that were determined, using as a marker the competitive antagonist α-bungarotoxin (Kubalek *et al*., 1987). In addition, the location of the cavities, ∼30 Å away from the membrane, was in agreement with data obtained from fluorescence resonance energy transfer measurements (Herz *et al*., 1989; Valenzuela *et al*., 1994).

The results presented here confirm that the cavities are approximately of the correct size and shape to accommodate an ACh molecule (Figure 11(a) and (c); Figure 12(c)). Furthermore, narrow tunnels about 10 to 15 Å long have now been resolved within the α subunits connecting the cavities to the water-filled vestibule of the channel (Figure 13). The tunnels very likely represent the primary routes by which ACh gains access to the binding sites, because the tunnel-cavity design parallels the ACh-binding region of the fast-acting enzyme, acetylcholinesterase, where there is a narrow "gorge" about 20 Å long widening out into the active site at its base (Sussman *et al*., 1991).

Figure 14. A 15 Å thick slab through the crescent of regular β-sheet densities framing the α_γ tunnel (same labelling as in Figure 13), and (superimposed) the α-carbon backbone tracings from the central portion of the twisted β-sheet strands that lie near the active site of acetylcholinesterase (strands: 2-8; Sussman *et al*., 1991; 2ACE coordinates from the Brookhaven Protein Data Bank). The slab is viewed from a direction approximately normal to the membrane plane; the densities and the α-carbon tracings fade towards the membrane surface.

Another aspect of structural similarity between the two proteins arises from comparison of the regular β-sheet densities framing the tunnels with the twisted β-sheet strands that lie adjacent to the active site of the enzyme. As Figure 14 shows, the receptor densities match closely a central seven-strand portion of the acetylcholinesterase motif (despite there being no detectable sequence homology of this region to the receptor).

Hence it appears that ACh is drawn into the ∼20 Å diameter vestibule of the channel, along with other cations, but may be selectively guided into the two binding pockets. In analogy with the case of acetylcholinesterase (Sussman *et al*., 1991; Ripoll *et al*., 1993), the guidance mechanism may entail a combination of electrostatic effects and interactions of the hydrophobic quaternary

ammonium group with aromatic residues lining the tunnel. Whether all the ACh and the cations enter (and leave) the channel through the mouth of the vestibule is not clear at the present resolution; it is quite likely, for example, that narrow openings between the subunits (such as the one next to α_γ in Figure 13), or within them, represent additional routes.

The structural picture of internal binding pockets accessed through narrow tunnels within the α subunits may provide a physical basis for the observation that inorganic monovalent cations compete for binding with agonists of the receptor (Akk & Auerbach, 1996). However, it is not easy to reconcile this picture with the interpretation, derived from chemical labelling and site-directed mutagenesis experiments, that the binding sites lie at the α-γ and α-δ subunit interfaces (Czajkowski & Karlin, 1995; Sine et al., 1995; Chiara & Cohen, 1997; Changeux & Edelstein, 1998). Equivalent interfaces of α_γ and α_δ with neighbouring subunits do not resemble one another at this level of the receptor, even though it is the level where binding occurs, according to the fluorescence resonance energy transfer measurements. On the other hand, the conformations of α_γ and α_δ (and hence their affinity for agonist) clearly are affected by their different interactions with neighbouring subunits, and this property of the three-dimensional structure is not taken into account when interpreting the mutagenesis results. It is also plausible that side-chains from the γ and δ subunits contribute to the structure shaping the tunnel entrances and/or cavities in the α subunits, and might therefore interact with ACh in its passage to the binding pocket.

Gate of the channel

In the open-channel form of the receptor, the pore would make a continuous water-filled passage from one side of the membrane to the other, narrowing towards the cytoplasmic surface (Villarroel et al., 1991; Lester, 1992). However, in this closed-channel form, a narrow strip of density bridges the pore at a level close to the middle of the membrane (Figure 11). This density, almost 15 Å away from the cytoplasmic membrane surface, must correspond to the gate of the channel, since it is the only region that would constitute a total barrier to the ions. The observed location coincides with the position of the gate indicated in the earlier structural study (Unwin, 1993), but differs from a location proposed on the basis of cysteine-substitution experiments involving amino acids in the loop between transmembrane segments M1 and M2 (Wilson & Karlin, 1998).

The width of the bridging density in Figure 11 appears to be less than a fifth of the separation of the phospholipid headgroups (i.e. <6 Å), suggesting that the gate is made from no more than one or two rings of side-chains. Evidently such a limited structure is sufficient, when framed by encircling subunits, to create a robust barrier to

ion permeation across the membrane. Given its location and its extent, the gate could well be an occlusion formed by conserved leucine side-chains projecting inwards from the middle of the transmembrane M2 segments of each of the subunits (Unwin, 1993). Involvement of these conserved leucine residues in gating has been suggested by the fact that their mutation, in increasing numbers, to polar residues increases markedly the opening sensitivity of the channel (Labarca et al., 1995; Filatov & White, 1995). However, paucity of polarisable groups together with restricted space for water would in themselves provide an unfavourable environment for the movement of ions, leaving open to question the precise physical nature of the gate.

Passages through the cytoplasmic wall

The cytoplasmic wall of the receptor was shown to contain openings wide enough for the ions to pass through, made by the spaces between ~30 Å long rods that protrude from each of the subunits towards the cell interior (Figure 12(a) and (b)). Interestingly, the spaces are not all equal in size, the widest being those on opposite faces of the two α subunits (arrows, Figure 12(b)) and the next widest those on either side of the intervening (β) subunit. However, the openings are all less than 10 Å across, and could therefore serve as filters to prevent most cytoplasmic anions (by repulsion from negatively charged side-chains), large cations and impermeant molecules from reaching the vicinity of the pore. The exclusion of anions from the cytoplasmic vestibule would facilitate transport through the transmembrane pore of small cations (mainly potassium ions) leaving the cell, since pairing interactions with counter-ions, which would compete with this process, are then avoided. (A similar role might be played by negatively charged side-chains lining the extracellular vestibule.)

The M3-M4 loop is responsible for most of the cytoplasmic mass of the ACh receptor (Popot & Changeux, 1984), and circumstantial evidence that the cytoplasmic structure does play a role in discriminating between ions of different charge can be obtained by comparing the relative numbers of negative and positive charge-carrying amino acid residues within this loop, for different members of the ACh receptor family. The net charge is negative for the cation-conducting ACh receptor, whereas it is positive for the anion-conducting glycine and GABA$_A$ receptors (Unwin, 1989). It is also possible to correlate the ~30 Å long rods with (α-helix-defining) heptad repeats of charged amino acids, the signs of which reflect the cation/anion selectivity of the channel. The ACh receptor α and β subunits from Torpedo, for example, have four successive negatively charged residues in the heptad positions (α: E377, E384, E391, E398; β: E406, E413, E420, D427; Noda et al., 1982, 1983); the glycine receptor α subunits from rat, on the other hand, have four successive positively charged resi-

dues in these positions (K371, K378, K385, R392; Grenningloh _et al._, 1987). (This heptad-containing stretch of sequence is in a conserved part of the M3-M4 loop nearest M4, and has been identified with a predicted amphipathic α-helix, once suggested to be lining the transmembrane pore (Finer-Moore & Stroud, 1984).)

Attachment to rapsyn

The central mass underlying the cytoplasmic vestibule of the receptor was interpreted in an earlier, lower resolution analysis of the tubular crystals to be composed entirely of non-receptor protein (Toyoshima & Unwin, 1988). This interpretation arose because the mass was absent in maps obtained from tubes frozen under conditions (pH 11) known to release the clustering protein, rapsyn (Neubig _et al._, 1979). Furthermore, tannic-acid-stained material was observed to be redistributed within the tubes after the alkaline treatment. However, rods can now be resolved protruding from each of the subunits and coming together on the receptor axis in the half of the central mass nearest the membrane surface. The earlier interpretation therefore was wrong. Apparently, it is only the half farthest from the membrane surface (which can be distinguished in radial density traces (Figure 9) and on the basis of symmetry (Figure 12(a), bottom)) that is likely to belong to rapsyn, and the cytoplasmic end of the receptor is not revealed by the high pH images because it becomes disordered and no longer contributes coherently to the structure determination.

The conclusion that rapsyn lies farther from the cytoplasmic membrane surface than the receptor is supported by ultrastructural studies of isolated _Torpedo_ postsynaptic membranes. For example, a continuous ''bar'' of density is seen, underlying the separately resolved receptors in tannic-acid-mediated negatively contrasted vesicles, which disappears after alkaline extraction (Sealock, 1982). In a freeze-etch study of the cytoplasmic face of the same membranes, the height of the protrusions made by the receptor-labelled particles was reduced, on average, by about 10 Å after alkaline extraction to remove the rapsyn-labelled component (Bridgman _et al._, 1987). However, only the receptor-attached portions of the 43 kDa rapsyn molecule appear to have been clearly visualised in the freeze-etch study and also in the structure described here. This might be because the rest of the molecule is flexible and becomes disorganised when detached from the cytoskeletal-anchored components with which it normally interacts (Apel _et al._, 1995, 1997). Also consistent with our results is the possibility that rapsyn dimers attach to different subunits (Maimone & Merlie, 1993), at the end of the receptor, and that the near 2-fold-related densities (Figure 12(a)) arise from particular orientations that have been reinforced by the crystallographic averaging.

Architecture of the sub-synaptic membrane

Figure 15 is a schematic drawing highlighting some functional aspects of the sub-synaptic membrane suggested by the structural results. Facing the synaptic cleft are the extracellular vestibules of the channels, which are wide enough to provide freely diffusing pathways for both the small inorganic cations and ACh. Opening into these vestibules are the tunnels, which selectively guide the ACh molecules to their binding sites. Near the middle of the membrane are the gate-forming amino acid side-chains. At the cytoplasmic membrane surface is the constriction zone made by the channels when they open. On the other side of the membrane, and next to the membrane surface, are passages in the channel walls for the cations to pass through. Further away, at the ends of the channels are the attached rapsyn molecules.

The sub-synaptic membrane can therefore be thought of as an assembly that is partitioned at different levels into a series of functional zones.
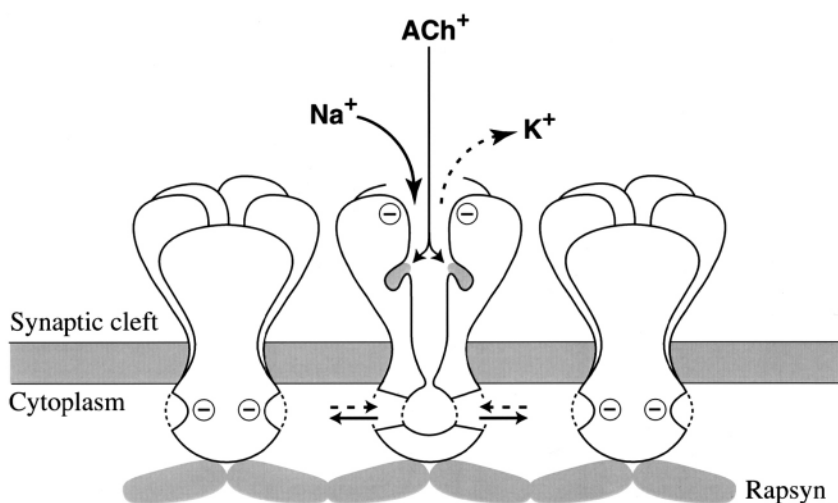

Figure 15. Architecture of the sub-synaptic membrane, depicting ACh binding and cation movement through an open channel. The results suggest that ACh molecules pass through the central vestibule of the channel before entering tunnels to their binding sites, and that cations leaving the cell interior are ''filtered'' through narrow openings in the channel wall. Framing these narrow openings are lines of negatively charged residues, which may help to exclude anions from the vicinity of the transmembrane pore.

One focus of this study has been the ~40 Å wide zone directly underneath the membrane, where cations enter and leave the channels, which is followed by the zone where rapsyn and presumably other cytoskeletal-anchored components interact. Such an organisation may be important in optimising side-by-side packing of the channels while retaining their full accessibility to cytoplasmic regulatory proteins and ions. Rapsyn, by attaching flexibly to the ends of the channels rather than between them, does not interfere with the close packing or obstruct the channel openings, and at the same time is located appropriately next to the underlying cytoskeleton. Partitioning of this nature may be a general property of cytoplasmic sub-synaptic structures, where it is necessary to achieve the highest possible concentrations of ion channels in order to maximise the postsynaptic response.

Outlook

The work reported here has combined a new method to determine structure from tubular crystals with the use of liquid helium temperatures to minimise radiation damage. This has allowed a resolution approaching atomic dimensions to be attained from only about 500,000 molecules: a limit that is primarily a result of the smallness in number of molecules analysed, according to the Fourier shell correlations (Figure 8). Since the resolution limit is not due to an inherent property of the specimen, such as short-range disorder, or to imaging deficiencies, which have been minimised by the use of a 300 kV field emission electron source, it should now be feasible to solve the atomic structure of the ACh receptor by further application of the same methods. Such a structure would furnish a precise three-dimensional framework on which to relate the findings of mutational experiments and a wide range of chemical and physical measurements.

The reduction in radiation damage achieved by the use of liquid helium has not been specifically investigated in our experiments. Quantitative estimation of signal loss as a function of electron dose is made difficult by the inability to record electron diffraction patterns of high quality from tubular crystals. However, it is notable that no inverse temperature factor weighting has been needed to sharpen the density maps to show clearly elements of secondary structure, as is usually the case with high resolution structure determinations where electron diffraction amplitudes are unavailable. Given that resolution-dependent signal loss would be contributed anyway by effects that have not been fully corrected (e.g. focus changes through the 800 Å thick specimen; unit cell variation associated with the different tube types), radiation damage cannot have played a major role. The tubes are protein/lipid shells enveloped by a large volume of amorphous ice, and it is plausible that they are exceptionally refractory to radiation damage at the very low temperatures. This could be due to an increased probability for recombination of hydrogen and hydroxyl radicals, and an inability of hydrogen to accumulate in the sample in the gaseous phase (Leapman & Sun, 1994).

At a more general level, the present study has demonstrated that tubular crystals offer a realistic alternative to two-dimensional crystals as a type of specimen suitable for high-resolution structure determination by electron microscopy. Two-dimensional crystals require tilting of the specimen to obtain the different views, and at high tilt angles high resolution is often difficult to achieve. Elimination of the need to tilt, the absence of a missing cone of information, and the facility by which membrane proteins and soluble proteins on lipid surfaces can be crystallised in tubular form (Wilson-Kubalek et al., 1998) are advantages that have potential for fuller exploitation in the future.

Methods

The specimen

Tubular crystals of about 800 Å in diameter were grown from postsynaptic membranes isolated from *Torpedo marmorata* electric organ in the standard way (Kubalek et al., 1987), using fish killed in the autumn or winter. The preparation involves no high salt or detergent treatment, and retains the native protein and lipid components of the postsynaptic membrane. While tubes could be obtained from most fish, only a small proportion of preparations gave high yields of tubes having the required dimensions and crystalline quality.

Sample preparation

Holey plastic films, containing closely spaced, 1-2 µm diameter holes, were prepared essentially as described by Fukami & Adachi (1965). They were overlaid on 300 mesh copper grids (Graticules Ltd.). Carbon (99.9999 % purity) was deposited onto the plastic-coated grids, with minimal sparking, using a standard carbon evaporator maintained at a vacuum of $<10^{-5}$ mbar during deposition (Fujiyoshi, 1998). The thicknesses of the carbon coats were such as to yield optical density values in the range 0.1-0.4 on glass slides placed next to the grids. The electrical resistivities of the coats were also monitored using an ohm-meter with probes spaced 2 cm apart and pressed hard against the slide. Typical measured resistances were 0.1-1.0 MΩ, which is one to two orders of magnitude lower than values often obtained for the same thicknesses under poorer vacuum conditions. Plastic was removed from the grids by immersing them completely in ethyl acetate (>20 minutes). Finally, the carbon-coated grids were irradiated intensely (3-4 hours; total dose ~100e/Å²; 100 kV electrons) in the projection chamber of a Philips EM301 electron microscope. This treatment not only improved the conductivity of the carbon by ~twofold (Figure 16(a)), but also appeared to strengthen and clean the support film, leading to greater reproducibility in the thickness and degree of spreading
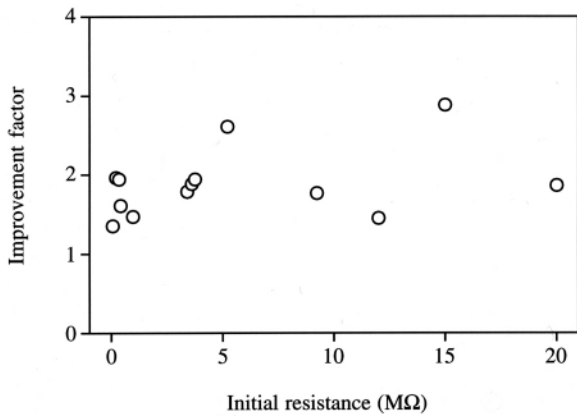
(a)
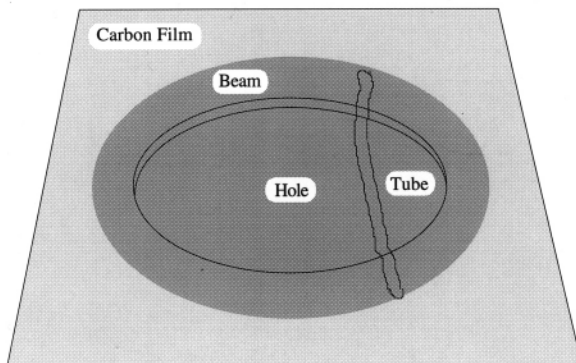
(b)

Figure 16. Sample preparation and microscopy. High conductivity, pre-irradiated carbon support grids and symmetrical illumination conditions helped to minimise beam-induced movement at the liquid helium temperatures. (a) The effect of pre-irradiation on conductivity of the carbon film. Carbon was evaporated onto glass cover-slips, which were placed on a copper block in the projection chamber of a Philips EM301 microscope, and strongly irradiated for four hours (total dose $\sim$100 e/Å^2). The improvement factor (initial resistance/final resistance) was $\sim$2 over a wide range of initial resistances (0.1-20 MΩ) generated by different film thicknesses (optical densities: 0.1-0.4) and evaporation conditions (2×10^{-6} to 5×10^{-5} mbar). The measured temperature rise during the irradiation was <15 deg. C, and there was no detectable change in optical density during the electron exposure. (b) The ideal illumination conditions for the ice-embedded sample, in which the beam diameter is slightly larger than the hole diameter and the beam is in contact with the carbon all the way round the hole: the middle of the hole, rather than the tube, is located at the centre of the micrograph.

of the ice films produced by the subsequent blotting and freezing steps (see below).

Freezing was done after the grids had been glow-discharged in the presence of amyl amine, using a plunging device housed in a high humidity chamber kept at 8 °C. Tube suspension (4.25 μl) was applied to the grid, held on the plunger, on the side away from the copper bars.

Excess solution was blotted off from the opposite side (Toyoshima, 1989), using no. 4A filter paper (Advantec), and as soon as the filter paper was observed to break contact with the solution on the grid, the grid was dropped by free-fall into liquid nitrogen-cooled ethane (~ -160 °C). Grids were stored under liquid nitrogen until ready for examination.

Microscopy

A JEM 3000SFF 300 kV field emission microscope, incorporating a top-entry liquid-helium cooled stage (Fujiyoshi et al., 1991; Fujiyoshi, 1998), was used to record images of tubes suspended in the amorphous ice over holes in the carbon support film. The images were taken at 40,000 × over a range of underfocus values (8500-18,000 Å), using low dose conditions ($\sim$20 e/Å^2). A clean 30 μm diameter gold foil objective aperture was always in place. The gold foil aperture, and the preparation of high conductivity carbon film, were important in minimising beam-induced movement caused by the increased resistance of the grid at 4 K. However, symmetrical imaging conditions, with the beam in contact with the carbon all the way around the hole (Figure 16(b)), were sometimes needed to eliminate movement altogether.

Selection of images and processing

Micrographs were screened initially by visual inspection and by optical diffraction in order to assess the overall quality of the tubes and select the appropriate helical families. Diffraction patterns from lengths boxed-off were required to display clear, sharp and symmetrical layer-lines, indicating that the tube was not grossly distorted and was properly embedded in the ice. Additionally, the contrast transfer function modulations in the background were required to be equally visible in all directions, indicating that there was little, if any, movement during the exposure. Most micrographs evaluated by these criteria were rejected because the tubes contained defects, were of the wrong family or were not ideally embedded in the ice. The remaining micrographs selected were digitised with a flatbed microdensitometer manufactured by Joyce, Loebl and Co., Ltd (extensively modified in-house), using a scanning interval and a spot size of 5.0 μm (corresponding to 1.3 Å on the specimen). The areas scanned included strips of ice on either side of the tube, to provide estimates of the background noise (see below), and the whole arrays were typically 10,000 pixels × 2200 pixels.

For three-dimensional structure determination, the tubes were treated as helical objects and analysed by dividing them into axial repeat lengths, each of which contains a complete set of views (DeRosier & Moore, 1970). Areas of tube were boxed off from the digitised images and interpolated in real space, so that (after refinement) an exact multiple of the axial repeat distance would be included in the Fourier transform (usually: 4096 × 2048). This made the layer-lines all fall exactly on the transform grid, while maintaining a constant sampling along the layer-lines ($1/(1.3 \times 2048)$ Å^{-1}) so that different images could be simply compared. A property of helical objects, and hence of the tubes, is that the Fourier terms from their near and far sides (corresponding to the sides nearest to and farthest from the electron source) are spatially separated. Individual near-side and far-side datasets were collected so that the different

focus levels could be taken into account in applying CTF corrections (see below).

Estimation of the CTF

Approximate defocus and astigmatism values for the images were determined by sector-averaging of the amplitudes in Fourier transforms calculated from the tubes, and by fitting of the averaged amplitudes in each sector to theoretical CTFs, assuming a value of 3 % for the amplitude contrast (Tani *et al.*, 1996). The CTF variation was refined following distortion correction by comparing the phases of the Fourier terms from the near and far sides of each tube, after applying CTF corrections, with those of the reference dataset. It was assumed that the focus levels of the two sides differed by 400 Å (i.e. by about half the tube diameter), and agreement was optimised for a range of CTF corrections around the estimated values (see also Figure 2(b)).

Distortion correction

Distortions were present in all tubes to varying extents. They consisted of changes of scale both along and perpendicular to the tube axis, variations in twist around this axis, bending in the image plane, and changes in out-of-plane tilt. To measure and to correct these distortions, the different helical families were considered separately. The repeat lengths along the tubes were divided into short segments, each segment was aligned independently in three dimensions to a reference dataset appropriate to the family in question, and the segments were added back together to reconstruct whole repeats after the misalignments had been removed.

All the manipulations were done in reciprocal space, with the reference dataset being derived each time from a fully corrected dataset obtained by combining the Fourier terms from all the previously analysed tubes. To calculate the reference dataset, the layer-lines of the fully corrected dataset were reassigned to match the helical selection rule of the tube being analysed (see below), and the terms along the layer-lines were multiplied by the CTF corresponding to the focus conditions used.

A description of the iterative procedure developed to achieve the segmental alignments has been given (Beroukhim & Unwin, 1997). In brief, the tube is first divided into (overlapping) portions, each corresponding to one axial repeat in length. The whole repeats are boxed-off and aligned against the reference dataset, using Fourier terms extending only to the first or second zero in the CTF. Next, the whole repeats are divided up into half-segments (of length approximately equal to the radius of the tube), and the half-segments are aligned against the reference dataset. Finally, the segments themselves, in orientations determined from the half-segment alignment, are refined against the reference dataset. Seven parameters are thus estimated for each successive segment: orientation in the image plane; out-of-plane tilt; effective repeat length; width relative to that of the reference; transverse, longitudinal and azimuthal alignments of the origin.

Combining datasets

The Fourier terms were extracted from the transforms of each segment, to the resolution limit, by treating the near- and far-side data separately. The terms from each side were combined vectorially to reconstruct repeat lengths, which in turn were combined to make near- and far-side datasets for the whole length of tube. The near- and far-side datasets for the whole length of tube were CTF-refined and corrected for the phase reversals (taking account of their different focus levels), and then combined to make a tube-averaged dataset. In combining the data at this step, the Fourier terms along the layer-lines, $F_{ij}(R,l)$ (where i refers to the tube and j to the side), were weighted by the CTF values, $|T_{ij}(R,l)|$, and the index, Q_{ij}, for the quality of each side (i.e. the number of phases in agreement with the centrosymmetric reference phases, minus those opposed, divided by the total number of comparisons):

$$F_i(R, l) = \frac{\sum_j Q_{ij} |T_{ij}(R, l)| F_{ij}(R, l)}{\sum_j Q_{ij}}$$

In practice, the values of Q_{ij} for the two sides differed by only a small amount (usually <20 %).

Finally, tube-averaged datasets were reassigned to one of the standard helical selection rules so that they could be combined vectorially to create the single, average dataset for the helical family in question. The final combined, CTF-corrected Fourier terms composing this dataset were given by:

$$F_c(R, l) = \frac{\sum_i N_i F_i(R, l)}{\sum_i N_i T_{ij}(R, l)^2}$$

with each image contributing according to the total number of segments, N_i, making up its length.

These formulae for combining images recorded under different focus conditions are similar to those used in earlier studies of ACh receptor tubes, and optimise the resultant signal-to-noise ratio (see e.g. Saxton, 1978). The weighting by number of segments favours appropriately subdivision of the images into shorter segments, where the distortions left uncorrected should be smaller. It is roughly equivalent to weighting by the number of receptors present, since the variation in segment length is fairly small (Tables 1 and 2).

Overlap of Bessel functions

In extracting the Fourier terms from the transforms of the tube segments, measurements were obtained along all layer-lines consistent with the helical symmetry at essentially all points out to the resolution limit. Many of the layer-lines therefore contained overlapping Bessel function peaks, especially at high resolution. However, the modifications made to the assigned Bessel terms by the interfering ones depend on the orientation of the tube, and therefore vary randomly from one specimen to the next. Also different patterns of overlap occur with different tubes because of slight variations in orientation of the surface lattice (leading to a range of tube types; see Figure 4). Thus we considered the effect of overlap to be a source of random error that should be averaged out after the Fourier terms from many datasets have been combined. The equivalence of the structures determined from the four helical families (see Results), which are quite distinct in terms of their overlap properties, confirms that the numbers of images averaged are sufficient to make this source of error unimportant.

Background noise

Accurate estimates of background noise were needed to evaluate the significance of each of the layer-line terms, many of which were extremely weak because of the continuous nature of the diffraction. The possibility of obtaining measurements from regions lying between the layer-lines (Morgan *et al.*, 1995) was discounted because many of the layer-lines lay adjacent to one another, especially at high resolution. Instead, therefore, the measurements were obtained from regions of ice adjacent to the tube, by computing the transforms and extracting amplitudes, $BKG_{ij}(R,l)$, at the layer-line positions (Beroukhim & Unwin, 1997). These background measurements were squared before summing and weighted as above. Thus:

$$BKG_i(R,l)^2 = \frac{\sum_j (Q_{ij} T_{ij}(R,l) BKG_{ij}(R,l))^2}{(\sum_j Q_{ij})^2}$$

and, after combining individual images:

$$BKG_c(R,l)^2 = \sum_i N_i^2 BKG_i(R,l)^2$$

Selection of Bessel peaks

The measurement of signal-to-noise ratio at each point along each layer-line, or *Point Quality* (*PQ*), was based on individual values for the amplitude, *F*, noise, *BKG*, and the phase, ϕ (ideally $0°$ or $180°$):

$$PQ(R,l) = \sqrt{\frac{2F(R,l)^2 \cos^2 \phi(R,l)}{BKG(R,l)^2}}$$

Fourier terms were considered insignificant and eliminated from the structure calculations if they were below background ($PQ < 1.0$). A further smaller set of terms was eliminated where the phases averaged locally, ϕ_m, did not yield close-to-centrosymmetric values. These terms were considered inconsistent with the fact that the Bessel modulations along the layer-lines are predominantly cosine waves, the peaks of which extend over ~1/800 Å, i.e. at least three successive transform points. All amplitudes retained were background-subtracted before performing the structure calculations, and the Bessel peaks were weighted by $|\cos\phi_m|$.

Equatorial layer-lines

The equatorial layer-line, contributed by the zero-order Bessel terms, gives information on the mean density of matter composing the tube as a function of radius. This layer-line was examined separately from the other layer-lines because it extends to very low resolution, where the (300 kV) contrast transfer is extremely weak, and is influenced disproportionately by small irregularities in the image, especially after the CTF corrections have been made. Examples of mean radial density distributions (g_{00}) calculated by Fourier-Bessel inversion of the terms from the averaged, CTF-corrected equatorial layer-lines of each family are given in Figure 9. The g_{00} values for the (−16,6) family were used in displaying the fully averaged structure, obtained from all the images.

Evaluation and structure calculations

Two kinds of criteria were use to measure the quality of the CTF and distortion-corrected images. The first was based on the index, Q_{ij}, indicating the level of agreement between the image dataset and the reference dataset (using all phases to a resolution of 10 Å). Images for which this index, averaged from both sides, was less than 0.17, were considered too poor for inclusion in the combined dataset.

The second measurement was independent of the reference dataset, and involved calculation of the 2-fold phase residual for the image, ϕ_i, in annuli of increasing resolution:

$$\phi_i = \frac{\sum F(R,l) \Delta\phi(R,l)}{\sum F(R,l)}$$

where $\Delta\phi(R,l)$ is the phase deviation from the nearest of $0°$ or $180°$. Images showing no evidence of signal (i.e. $\phi_i \cong 45°$) beyond 20 Å resolution by this criterion were also rejected.

For the structure calculations, the real components of the layer-line terms were first incorporated in a Fourier-Bessel inversion to make a Table of the strengths of the helical density waves associated with each layer-line (g_{nl}), as a function of radius. The minor signal losses associated with distortions remaining uncorrected over sub-segment lengths were compensated at the same time by multiplying the g_{nl} terms by $1/\cos(2\pi\delta d/d)$, where d is the resolution and δd is the effective displacement error (estimated to be 0.75 Å). Three-dimensional maps were then calculated from the Table by Fourier synthesis in sections both parallel and perpendicular to the axis of the tube (Klug *et al.*, 1958; DeRosier & Moore, 1970). The maps were displayed in three dimensions using the crystallographic programs O (Jones *et al.*, 1991) and SETOR (Evans, 1993).

To evaluate the reliability and resolution of the structures determined from the different helical families, single receptors were isolated from the three-dimensional maps, aligned by a correlation search (see Results), and compared by Fourier shell correlation and phase residual measurements (van Heel, 1987; Böttcher *et al.*, 1997). All these manipulations, and averaging of structures to obtain a final map, were done on successive 1 Å spaced sections parallel to the axis of the tube (i.e. perpendicular to the axis of the receptor). Cylindrical masks (cut-off radius: 45 Å) were used to isolate the single receptor from each of the maps and for most of the calculations the masked-out receptors were incorporated in 128 Å side-length cubes.

References

Akk, G. & Auerbach, A. (1996). Inorganic, monovalent cations compete with agonists for the transmitter binding site of nicotinic acetylcholine receptors. *Biophys. J.* **70**, 2652-2658.

Apel, E. D., Roberds, S. L., Campbell, K. P. & Merlie, J. P. (1995). Rapsyn may function as a link between the acetylcholine receptor and the agrin-binding dystrophin-associated glycoprotein complex. *Neuron,* **15**, 115-126.

Apel, E. D., Glass, D. J., Moscoso, L. M., Yancopoulos, G. D. & Sanes, J. R. (1997). Rapsyn is required for MuSK signaling and recruits synaptic components to a MuSK-containing scaffold. *Neuron,* **18**, 623-625.

Beroukhim, R. & Unwin, N. (1997). Distortion correction of tubular crystals: improvements in the acetylcholine receptor structure. *Ultramicroscopy,* **70**, 57-81.

Böttcher, B., Wynne, S. A. & Crowther, R. A. (1997). Determination of the fold of the core protein of hepatitis B virus by electron cryomicroscopy. *Nature,* **386**, 88-91.

Bridgman, P. C., Carr, C., Pederson, S. E. & Cohen, J. B. (1987). Visualization of the cytoplasmic surface of *Torpedo* postsynaptic membranes by freeze-etch and immunoelectron microscopy. *J. Cell Biol.* **105**, 1829-1846.

Brisson, A. & Unwin, P. N. T. (1984). Tubular crystals of acetylcholine receptor. *J. Cell Biol.* **99**, 1202-1211.

Changeux, J.-P. & Edelstein, S. J. (1998). Allosteric receptors after 30 years. *Neuron,* **21**, 959-980.

Chiara, D. C. & Cohen, J. B. (1997). Identification of amino acids contributing to high and low affinity *d*-tubocurarine sites in the *Torpedo* nicotinic acetylcholine receptor. *J. Biol. Chem.* **272**, 32940-32950.

Czajkowski, C. & Karlin, A. (1995). Structure of the nicotinic receptor acetylcholine-binding site. Identification of acidic residues in the δ subunit within 0.9 nm of the α-subunit-binding disulfide. *J. Biol. Chem.* **270**, 3160-3164.

DeRosier, D. J. & Moore, P. B. (1970). Reconstruction of three-dimensional images from electron micrographs of structures with helical symmetry. *J. Mol. Biol.* **52**, 355-369.

DeRosier, D. J., Stokes, D. L. & Darst, S. A. (1999). Averaging data derived from images of helical structures with different symmetries. *J. Mol. Biol.* in the press.

Evans, S. V. (1993). SETOR: hardware lighted three-dimensional solid model representations of macromolecules. *J. Mol. Graph.* **11**, 134-138.

Filatov, G. N. & White, M. M. (1995). The role of conserved leucines in the M2 domain of the acetylcholine receptor in channel gating. *Mol. Pharmacol.* **48**, 379-384.

Finer-Moore, J. & Stroud, R. M. (1984). Amphipathic analysis and possible formation of the ion channel in an acetylcholine receptor. *Proc. Natl Acad. Sci. USA,* **81**, 155-159.

Fukami, A. & Adachi, K. (1965). A new method of preparation of a self-perforated micro plastic grid and its application. *J. Electron Microsc.* **14**, 112-118.

Fujiyoshi, Y. (1998). The structural study of membrane proteins by electron crystallography. *Advan. Biophys.* **35**, 27-74.

Fujiyoshi, Y., Mizusaki, T., Morikawa, K., Yamagishi, H., Aoki, Y., Kihara, H. & Harada, Y. (1991). Development of a superfluid helium stage for high resolution electron microscopy. *Ultramicroscopy,* **38**, 241-251.

Grenningloh, G., Rienitz, A., Schmitt, B., Methfessel, C., Zensen, M., Beyreuther, K., Gundelfinger, E. D. & Betz, H. (1987). The strychnine-binding subunit of the glycine receptor shows homology with nicotinic acetylcholine receptors. *Nature,* **328**, 215-220.

Herz, J. M., Johnson, D. A. & Taylor, P. (1989). Distance between agonist and noncompetitive inhibitor sites on the nicotinic acetylcholine receptor. *J. Biol. Chem.* **264**, 12439-12448.

Heuser, J. E. & Salpeter, S. R. (1979). Organization of acetylcholine receptors in quick-frozen, deep-etched, and rotary-replicated *Torpedo* postsynaptic membrane. *J. Cell Biol.* **82**, 150-173.

Jones, T. A., Zhou, J. Y., Cowan, S. W. & Kjeldgaard, M. (1991). Improved methods for building protein models in electron density maps and the location of errors in these models. *Acta Crystallog. sect. A,* **47**, 110-119.

Karlin, A. (1993). Structure of nicotinic acetylcholine receptors. *Curr. Opin. Neurobiol.* **3**, 299-309.

Karlin, A. & Akabas, M. H. (1995). Toward a structural basis for the function of nicotinic acetylcholine receptors. *Neuron,* **15**, 1231-1244.

Klug, A., Crick, F. H. C. & Wykoff, H. W. (1958). Diffraction by helical structures. *Acta Crystallog.* **11**, 199-213.

Kubalek, E., Ralston, S., Lindstrom, J. & Unwin, N. (1987). Location of subunits within the acetylcholine receptor by electron image analysis of tubular crystals from *Torpedo marmorata*. *J. Cell Biol.* **105**, 9-18.

Labarca, C., Nowak, M. W., Zhang, H., Tang, L., Deshpande, P. & Lester, H. A. (1995). Channel gating governed symmetrically by conserved leucine residues in the M2 domain of nicotinic receptors. *Nature,* **376**, 514-516.

LaRochelle, W. J. & Froehner, S. C. (1986). Determination of the tissue distributions and relative concentrations of the postsynaptic 43-kDa protein and the acetylcholine receptor in *Torpedo*. *J. Biol. Chem.* **261**, 5270-5274.

Leapman, R. D. & Sun, S. (1994). Cryo-electron energy loss spectroscopy: observations on vitrified hydrated specimens and radiation damage. *Ultramicroscopy,* **59**, 71-79.

Lester, H. A. (1992). The permeation pathway of neurotransmitter-gated ion channels. *Annu. Rev. Biophys. Biomol. Struct.* **21**, 267-292.

Maimone, M. M. & Merlie, J. P. (1993). Interaction of the 43 kd postsynaptic protein with all subunits of the muscle nicotinic acetylcholine receptor. *Neuron,* **11**, 53-66.

Morgan, D. G., Owen, C., Melanson, L. A. & DeRosier, D. J. (1995). Structure of bacterial flagellar filaments at 11 Å resolution: packing of the α-helices. *J. Mol. Biol.* **249**, 88-110.

Neubig, R. R. & Cohen, J. B. (1979). Equilibrium binding of [³H]tubocurarine and [³H]acetylcholine by *Torpedo* postsynaptic membranes: stoichiometry and ligand interactions. *Biochemistry,* **18**, 5464-5475.

Neubig, R. R., Krodel, E. K., Boyd, N. D. & Cohen, J. B. (1979). Acetylcholine and local anaesthetic binding to *Torpedo* nicotinic post-synaptic membranes after removal of non-receptor peptides. *Proc. Natl Acad. Sci. USA,* **76**, 690-694.

Noda, M., Takahashi, H., Tanabe, T., Toyosatao, M., Furutani, Y., Hirose, T., Asai, M., Inayama, S., Miyata, T. & Numa, S. (1982). Primary structure of

the α-subunit precursor of *Torpedo californica* acetylcholine receptor deduced from cDNA sequence. *Nature*, **299**, 793-797.

Noda, M., Takahashi, H., Tanabe, T., Toyosatao, M., Kikyotani, Y., Hirose, T., Asai, M., Takashima, H., Inayama, S., Miyata, T. & Numa, S. (1983). Primary structures of β- and δ-subunit precursors of *Torpedo californica* acetylcholine receptor deduced from cDNA sequences. *Nature*, **301**, 251-255.

Popot, J.-L. & Changeux, J.-P. (1984). Nicotinic receptor of acetylcholine: structure of an oligomeric membrane protein. *Physiol. Rev.* **64**, 1162-1239.

Ripoll, D. R., Faerman, C. H., Axelsen, P. H., Silman, I. & Sussman, J. L. (1993). An electrostatic mechanism for substrate guidance down the aromatic gorge of acetylcholinesterase. *Proc. Natl Acad. Sci. USA,* **90**, 5128-5132.

Saxton, W. O. (1978). *Computer Techniques for Image Processing in Electron Microscopy*, Academic Press, New York.

Sealock, R. (1982). Cytoplasmic surface structure in post-synaptic membranes from electric tissue visualized by tannic-acid-mediated negative contrasting. *J. Cell Biol.* **92**, 514-522.

Sine, S. M., Kreienkamp, H.-J., Bren, N., Maeda, R. & Taylor, P. (1995). Molecular dissection of subunit interfaces in the acetylcholine receptor: identification of determinants of α-conotoxin M1 selectivity. *Neuron,* **15**, 205-211.

Sussman, J. L., Harel, M., Frolow, F., Oefner, C., Goldman, A., Toker, L. & Silman, I. (1991). Atomic structure of acetylcholinesterase from *Torpedo californica:* a prototypic acetylcholine-binding protein. *Science,* **253**, 872-878.

Tani, K., Sasabe, H. & Toyoshima, C. (1996). A set of computer programs for determining defocus and astigmatism in electron images. *Ultramicroscopy,* **65**, 31-44.

Toyoshima, C. (1989). On the use of holey grids in electron crystallography. *Ultramicroscopy,* **30**, 439-444.

Toyoshima, C. & Unwin, N. (1988). Ion channel of acetylcholine receptor reconstructed from images of postsynaptic membranes. *Nature,* **336**, 247-250.

Toyoshima, C. & Unwin, N. (1990). Three-dimensional structure of the acetylcholine receptor by cryoelectron microscopy and helical image reconstruction. *J. Cell Biol.* **111**, 2623-2635.

Unwin, N. (1989). The structure of ion channels in membranes of excitable cells. *Neuron,* **3**, 665-676.

Unwin, N. (1993). Nicotinic acetylcholine receptor at 9 Å resolution. *J. Mol. Biol.* **229**, 1101-1124.

Unwin, N. (1995). Acetylcholine receptor channel imaged in the open state. *Nature,* **373**, 37-43.

Unwin, N. (1996). Projection structure of the nicotinic acetylcholine receptor: distinct conformations of the α subunits. *J. Mol. Biol.* **257**, 586-596.

Valenzuela, C. F., Weign, P., Yguerabide, J. & Johnson, D. A. (1994). Transverse distance between the membrane and the agonist binding sites on the *Torpedo* acetylcholine receptor: a fluorescence study. *Biophys. J.* **66**, 674-682.

van Heel, M. (1987). Similarity measures between images. *Ultramicroscopy,* **21**, 95-100.

Villarroel, A., Herlitze, S., Koenen, M. & Sakmann, B. (1991). Location of a threonine residue in the α-subunit M2 transmembrane segment that determines the ion flow through the acetylcholine receptor channel. *Proc. Roy. Soc., ser. B,* **243**, 69-74.

Wilson, G. G. & Karlin, A. (1998). The location of the gate in the acetylcholine receptor channel. *Neuron,* **20**, 1269-1281.

Wilson-Kubalek, E. M., Brown, R. E., Celia, H. & Milligan, R. A. (1998). Lipid nanotubes as substrates for helical crystallization of macromolecules. *Proc. Natl Acad. Sci. USA,* **95**, 8040-8045.